

SUPPORTING INFORMATION

Quantum Interference dependence on molecular configurations for cross-conjugated systems in single-molecule junctions

Juan Hurtado-Gallego^{1, ‡}, Ross Davidson^{2, ‡}, Iain M. Grace^{3, ‡}, Laura-Rincón-García¹, Andrei S.

*Batsanov², Martin R. Bryce^{2, *}, Colin J. Lambert^{3, *} and Nicolás Agrait^{1, 4, 5, *}*

¹Departamento de Física de la Materia Condensada, Universidad Autónoma de Madrid, E-28049 Madrid, Spain

²Department of Chemistry, Durham University, Durham DH1 3LE, United Kingdom

³Physics Department, Lancaster University, Lancaster, LA1 4YB, United Kingdom

⁴Condensed Matter Physics Center (IFIMAC) and Instituto Universitario de Ciencia de Materiales ‘Nicolás Cabrera’ (INC), Universidad Autónoma de Madrid, E-28049 Madrid, Spain

⁵Instituto Madrileño de Estudios Avanzados en Nanociencia IMDEA-Nanociencia, E-28049 Madrid, Spain

‡Authors with equal contributions.

Corresponding Authors: nicolas.agrait@uam.es; m.r.bryce@durham.ac.uk; c.lambert@lancaster.ac.uk

Table of Contents

a) Experimental

S1. Synthesis and characterisation of target compounds	S3
S2. NMR spectra of reported compounds	S12
S3. Crystallographic data	S21
S4. Photophysical measurements	S24
S5. Conductance measurements	S26
S6. Seebeck coefficient measurements	S32

b) Theoretical

S7. Theoretical Methods	S34
S8. Molecular orbitals	S35
S9. Energy levels, ionization potential and electron affinity	S38
S10. Binding energies	S39
S11. Transmission coefficients	S44
S12. Conductance and Seebeck coefficient calculations for configuration 1	S50
S13. Conductance calculations for configuration 2	S57

c) References for SI	S60
----------------------	-----

a) Experimental

Instrumentation. NMR spectra were recorded in deuterated solvent solutions on a Varian VNMRS-600 spectrometer and referenced against solvent resonances (^1H , ^{13}C).

ASAP data were recorded on a Xevo Q-TOF (Waters) high resolution accurate mass tandem mass spectrometer equipped with Atmospheric Pressure Gas Chromatography (APGC) and Atmospheric Solids Analysis Probe (ASAP). Microanalyses were performed by Elemental Microanalysis Service, Durham University, UK.

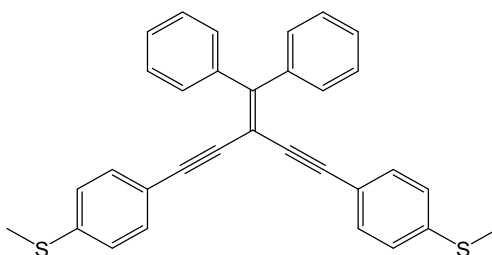
S1. Synthesis and characterisation of target compounds

General details. All chemicals were sourced from standard chemical suppliers, with the exception of (2,2-dibromoethene-1,1-diyl)dibenzene¹, 9-(dibromomethylene)-9H-fluorene², 9-(dibromomethylene)-9H-thioxanthene³, (2-((4-ethynylphenyl)thio)ethyl)trimethylsilane⁴, and (4-ethynylphenyl)(methyl)sulfane⁵ which were prepared following literature methods.

General method for (4-ethynylphenyl)(methyl)sulfane Sonogashira coupling.

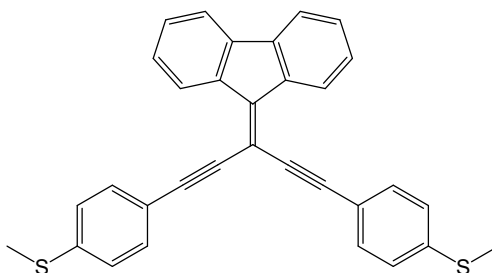
$\text{Pd}(\text{PPh}_3)_4$ (0.2 eq, 231 mg, 0.20 mmol) and CuI (0.2 eq, 38 mg, 0.20 mmol) were added to a freeze-pump-thaw degassed solution containing (2,2-dibromoethene-1,1-diyl)dibenzene (1 eq, 1.18 mmol), (4-ethynylphenyl)(methyl)sulfane (2 eq, 349 mg, 2.36 mmol), Et_3N (5 mL) and tetrahydrofuran (THF; 40 mL). The solution was heated under reflux for 48 h before the solvent was removed. Purification was achieved via column chromatography on silica eluted by a solvent gradient from neat hexane to $\text{DCM}:\text{hexane}$ (1:1 v/v), to produce the desired product.

((3-(diphenylmethylene)penta-1,4-diyne-1,5-diyl)bis(4,1-phenylene))bis(methylsulfane) (**1a**).



Yield: 83 mg (15%). **¹H-NMR** (CD₂Cl₂, 600 MHz) δ_H 7.54-7.53 (m, 4H, H_c), 7.42-7.37 (m, 6H, H_a+H_b), 7.24 (d, ³J_{HH} = 7.8 Hz, 4H, H_e), 7.18 (d, ³J_{HH} = 7.8 Hz, 4H, H_d), 2.49 (s, 6H, H_f) ppm. **¹³C{¹H}-NMR** (CD₂Cl₂, 126 MHz) δ_C 155.5, 140.3, 139.9, 131.5, 130.3, 128.5, 127.6, 125.5, 118.9, 101.8, 91.4, 88.5, 14.9 ppm. **Acc-MS** (ASAP⁺): *m/z* 473.1416 [M+H]⁺, calcd. for C₃₂H₂₅S₂ *m/z* 473.1436 (|Δ*m/z*| = 3.8 ppm), **Anal. Calc.** for C₃₂H₂₄S₂·½H₂O: C, 79.80; H, 5.23 %. **Found:** C, 79.58; H, 5.20 %.

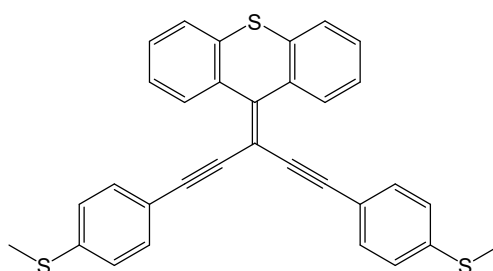
((3-(9H-fluoren-9-ylidene)penta-1,4-diyne-1,5-diyl)bis(4,1-phenylene))bis(methylsulfane) (**2a**).



Yield: 211 mg (38%). **¹H-NMR** (CD₂Cl₂, 600 MHz) δ_H 8.72 (dt, ³J_{HH} = 7.8 Hz, ⁴J_{HH} = 0.9 Hz, 2H, H_a), 7.73 (dt, ³J_{HH} = 7.4 Hz, ⁴J_{HH} = 1.0 Hz, 2H, H_d), 7.60 (d, ³J_{HH} = 8.0 Hz, 4H, H_f), 7.42 (td, ³J_{HH} = 7.4 Hz, ⁴J_{HH} = 1.1 Hz, 2H, H_c), 7.36 (td, ³J_{HH} = 7.6 Hz, ⁴J_{HH} = 1.2 Hz, 2H, H_b), 7.31 (d, ³J_{HH} = 8.0 Hz, 4H, H_e), 2.55 (s, 6H, H_g) ppm. **¹³C{¹H}-NMR** (CD₂Cl₂, 126 MHz) δ_C 144.4, 141.1, 140.0, 137.3, 131.9, 129.5, 127.4, 125.6, 125.2, 119.6, 118.5, 101.2, 97.9,

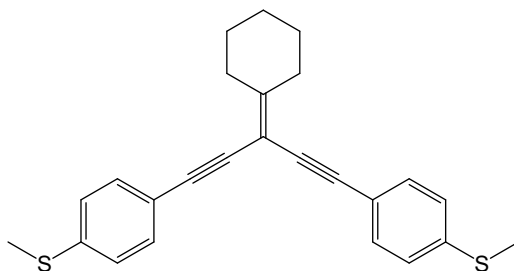
88.8, 14.9 ppm. **Acc-MS** (ASAP⁺): m/z 471.1245 [M+H]⁺, calcd. for C₃₂H₂₃S₂ m/z 471.1241 ($|\Delta m/z| = 0.8$ ppm), **Anal. Calc.** for C₃₂H₂₂S₂: C, 81.66; H, 4.71 %. **Found:** C, 81.51; H, 4.64 %.

9-(1,5-bis(4-(methylthio)phenyl)penta-1,4-diyne-3-ylidene)-9H-thioxanthene (3a)



Yield: 282 mg (26%). **¹H-NMR** (CD₂Cl₂, 600 MHz) δ_{H} 8.24 (dd, ³ $J_{\text{HH}} = 7.9$ Hz, 1.8 Hz, 2H, H_a), 7.55 (dd, ³ $J_{\text{HH}} = 7.9$ Hz, ⁴ $J_{\text{HH}} = 1.7$ Hz, 2H, H_d), 7.41-7.34 (m, 8H, H_b+H_c+H_f), 7.21 (d, ³ $J_{\text{HH}} = 8.0$ Hz, 4H, H_e), 2.51 (s, 6H, H_g) ppm. **¹³C{¹H}-NMR** (CD₂Cl₂, 126 MHz) δ_{C} 146.0, 140.3, 133.7, 133.5, 131.6, 129.1, 128.1, 126.0, 125.6, 125.4, 118.8, 102.4, 92.1, 88.2, 14.9 ppm. **Acc-MS** (ASAP⁺): m/z 503.0959 [M+H]⁺, calcd. for C₃₂H₂₃S₃ m/z 503.0962 ($|\Delta m/z| = 0.3$ ppm), **Anal. Calc.** for C₃₂H₂₂S₃: C, 76.46; H, 4.41 %. **Found:** C, 76.36; H, 4.45 %.

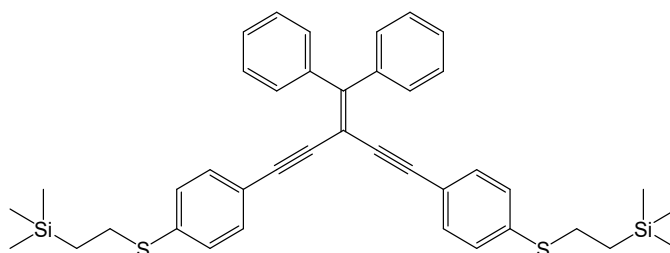
((3-cyclohexylidenepenta-1,4-diyne-1,5-diyl)bis(4,1-phenylene))bis(methylsulfane) (4).



(3-cyclohexylidenepenta-1,4-diyne-1,5-diyl)bis(trimethylsilane) (500 mg, 1.73 mmol) was added to a solution containing KF (203 mg, 3.5 mmol) in methanol (50 mL), the solution was stirred for 2 min before the solution was extracted with diethyl ether and water, and the organic fractions were collected and dried over MgSO₄ and filtered. The solvent was removed from the filtrate at room temperature under vacuum. The residue was dissolved in THF (50 mL) and Et₃N (5 mL) and 4-iodothioanisole (875 mg, 3.5 mmol) added, the solution was degassed by three freeze-pump-thaw cycles before CuI (32 mg, 0.17 mmol) and Pd(PPh₃)₄ (196 mg, 0.17 mmol) were added. The solution was stirred overnight before the solvent was removed. The product was purified via silica chromatography eluted by a solvent gradient from neat hexane to DCM:hexane (1:1 v/v) to give a white solid. **Yield:** 275 mg (41%). **¹H-NMR** (CD₂Cl₂, 600 MHz) δ_H 7.39 (d, ³J_{HH} = 8.2 Hz, 4H, H_b), 7.20 (d, ³J_{HH} = 8.2 Hz, 4H, H_a), 2.64-2.62 (m, 4H, H_c), 2.49 (s, 6H, H_f), 1.69-1.61 (m, 6H) ppm. **¹³C{¹H}-NMR** (CD₂Cl₂, 126 MHz) δ_C 161.5, 139.3, 131.5, 125.6, 119.4, 97.6, 90.6, 85.9, 32.8, 27.7, 26.1, 15.0 ppm. **Acc-MS** (ASAP⁺): *m/z* 389.1397 [M+H]⁺, calcd. for C₂₅H₂₅S₂ *m/z* 389.1398 (|Δ*m/z*| = 0.3 ppm). **Anal. Calc.** for C₂₅H₂₄S₂·½H₂O: C, 75.52; H, 6.34 %. **Found:** C, 75.88; H, 6.21 %.

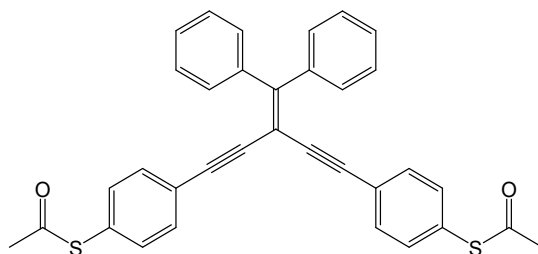
General method for (2-((4-ethynylphenyl)thio)ethyl)trimethylsilane Sonogashira coupling. Pd(PPh₃)₄ (0.2 eq, 231 mg, 0.20 mmol) and CuI (0.2 eq, 38 mg, 0.20 mmol) were added to a freeze-pump-thaw degassed solution containing (2,2-dibromoethene-1,1-diyl)dibenzene (1 eq, 1.18 mmol), (2-((4-ethynylphenyl)thio)ethyl)trimethylsilane (2 eq, 745 mg, 2.36 mmol), Et₃N (5 mL) and THF (40 mL). The solution was heated to reflux for 48 h before the solvent was removed. Purification was achieved via column chromatography on silica eluted by a solvent gradient from neat hexane to DCM:hexane (1:1 v/v), to yield the TMS protected intermediates. Where the intermediate species could be isolated as a pure species it was characterised. Each of the vinyl TMS protected compounds were deprotected by adding tetrabutylammonium fluoride (5 eq, 1.0 M) to a solution of the vinyl-TMS intermediate (1 eq) in THF (30 mL), immediately resulting in a colour change. The solution was stirred for 1 h before acetyl chloride (7 eq) was added, turning the solution colourless. Stirring was continued for an additional 4 h before the reaction was quenched with water and extracted with DCM. The combined organic fractions were dried over MgSO₄ before removing the solvent. Purification was achieved by column chromatography on silica eluted by a solvent gradient from DCM:hexane (1:1 v/v) to neat DCM.

(((3-(diphenylmethylene)penta-1,4-diyne-1,5-diyl)bis(4,1-phenylene))bis(sulfanediyl))bis(ethane-2,1-diyl))bis(trimethylsilane) (Ph₂-STMS₂).



A colourless oil, that solidifies to a waxy solid upon standing. **Yield:** 130 mg (14%). **¹H-NMR** (CDCl₃, 600 MHz) δ_H 7.52 (dd, ³J_{HH} = 7.7 Hz, ⁴J_{HH} = 1.9 Hz, 4H, H_c), 7.38-7.32 (m, 6H, H_d+H_e), 7.21 (d, ³J_{HH} = 8.3 Hz, 4H, H_a), 7.16 (d, ³J_{HH} = 8.3 Hz, 4H, H_b), 2.98-2.93 (m, 4H, H_f), 0.95-0.90 (m, 4H, H_g), 0.03 (s, 18H, H_h) ppm. **¹³C{¹H}-NMR** (CDCl₃, 126 MHz) δ_C 155.42, 140.43, 138.41, 132.65, 131.69, 130.46, 128.44, 127.61, 119.92, 109.99, 91.58, 89.00, 28.91, 16.62, -1.79 ppm. **Acc-MS** (ASAP⁺): *m/z* 645.2501 [M+H]⁺, calcd. for C₄₀H₄₅S₂Si₂ (|Δ*m/z*| = 1.2 ppm). **Anal. Calc.** for C₄₀H₄₄S₂Si₂: C, 74.48; H, 6.88 % %. **Found:** C, 74.83; H, 6.95 %.

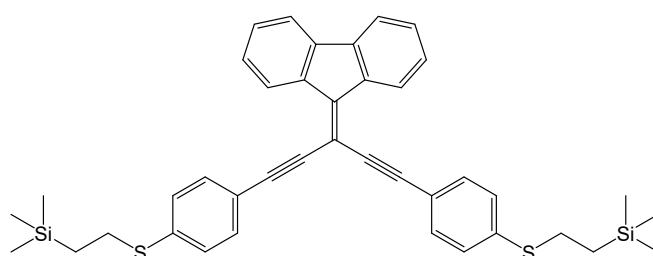
S,S'-((3-(diphenylmethylene)penta-1,4-diyne-1,5-diyl)bis(4,1-phenylene)) diethanethioate (**1b**).



A white solid. **Yield:** 33 mg (42%). **¹H-NMR** (CDCl₃, 600 MHz) δ 7.52-7.51 (m, 4H, H_c), 7.38-7.36 (m, 6H, H_d+H_e), 7.33-7.31 (m, 8H, H_a+H_b), 2.41 (s, 6H, H_f) ppm. **¹³C{¹H}-NMR**

(CDCl₃, 126 MHz) δ_C 193.39, 157.19, 140.18, 134.08, 131.99, 130.43, 128.75, 128.08, 127.71, 124.30, 101.49, 90.99, 90.16, 30.25 ppm. **Acc-MS (ASAP⁺):** m/z 529.1289 [M+H]⁺, calcd. for C₃₄H₂₅O₂S₂ ($|\Delta m/z| = 1.3$ ppm).ⁱ

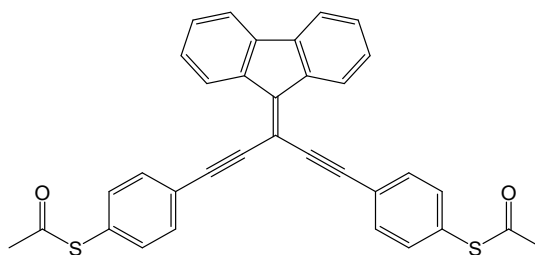
(((3-(9H-fluoren-9-ylidene)penta-1,4-diyne-1,5-diyl)bis(4,1-phenylene))bis(sulfanediy))bis(ethane-2,1-diyl))bis(trimethylsilane) (Fluorene-STMS₂).



Final purification was achieved by recrystallisation through evaporation of a MeOH/DCM solution to give orange crystals. **Yield:** 523 mg (68%). **¹H-NMR** (CDCl₃, 600 MHz) δ_H 8.68 (dt, ³ $J_{HH} = 7.79$ Hz, ⁴ $J_{HH} = 0.98$ Hz, 2H, H_f), 7.67 (dt, ³ $J_{HH} = 7.45$, ⁴ $J_{HH} = 0.98$ Hz, 2H, H_c), 7.55 (d, ³ $J_{HH} = 8.3$ Hz, 4H, H_a), 7.37 (td, ³ $J_{HH} = 7.33$, ⁴ $J_{HH} = 0.98$ Hz, 2H, H_d), 7.31-7.28 (m, 6H, H_b+H_e), 3.06-3.00 (m, 4H, H_g), 1.00-0.95 (m, 4H, H_h), 0.07 (s, 18H, H_i) ppm. **¹³C{¹H}-NMR** (CDCl₃, 126 MHz) δ_C 144.67, 140.15, 139.71, 137.49, 131.98, 129.39, 127.62, 127.42, 125.36, 119.55, 119.37, 101.36, 97.81, 89.23, 28.75, 16.60, -1.77 ppm. **MS(ASAP):** m/z 644.242 [M+H]⁺. **Anal. Calc.** for C₄₀H₄₂S₂Si₂: C, 74.71; H, 6.58 %. **Found:** C, 74.39; H, 6.48 %.

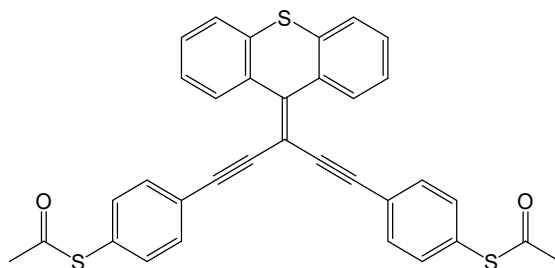
S,S'-((3-(9H-fluoren-9-ylidene)penta-1,4-diyne-1,5-diyl)bis(4,1-phenylene)) diethanethioate (2b).

ⁱ Repeated elemental analysis gave low carbon values.



Final purification was achieved by recrystallisation through evaporation of a MeOH/DCM solution to give orange crystals. **Yield:** 65 mg (39%). **¹H-NMR** (CDCl₃, 600 MHz) δ 8.64 (d, ³J_{HH} = 7.8 Hz, 2H, H_f), 7.68-7.66 (m, 6H, H_a+H_c), 7.47 (d, ³J_{HH} = 8.0 Hz, 4H, H_b), 7.38 (td, ³J_{HH} = 7.6 Hz, ⁴J_{HH} = 1.2 Hz, 2H, H_d), 7.31 (td, ³J_{HH} = 7.6 Hz, ⁴J_{HH} = 1.2 Hz, 2H, H_e), 2.46 (s, 6H, H_g) ppm. **¹³C{¹H}-NMR** (CDCl₃, 126 MHz) δ: 193.1, 146.0, 140.3, 137.3, 134.3, 132.2, 129.8, 129.1, 127.6, 125.5, 123.8, 119.6, 100.4, 96.9, 90.1, 30.3 ppm. **MS(ASAP):** *m/z* 527.115 [M+H]⁺, **Acc-MS** (ASAP⁺): *m/z* 526.1071[M]⁺, calcd. for C₃₄H₂₂O₂S₂ ($|\Delta m/z| = 1.9$ ppm), **Anal. Calc.** for C₃₄H₂₂O₂S₂: C, 77.86; H, 4.56 %. Found: C, 77.54; H, 4.21 %.

((3-(9H-thioxanthen-9-ylidene)penta-1,4-diyne-1,5-diyl)bis(4,1-phenylene)) diethanethioate
(3b).



A yellow solid. **Yield:** 113 mg (37%). **¹H-NMR** (CD₂Cl₂, 600 MHz) δ 8.24 (dd, ³J_{HH} = 7.6 Hz, ⁴J_{HH} = 1.7 Hz, 2H, H_d), 7.56 (d, ³J_{HH} = 7.65 Hz, 2H, H_a), 7.47 (d, ³J_{HH} = 8.0 Hz, 4H, H_f), 7.42-7.36 (m, 8H, H_b+H_c+H_e), 2.42 (s, 6H, H_g) ppm. **¹³C{¹H}-NMR** (CD₂Cl₂, 126 MHz) δ: 193.1, 134.3, 133.5, 133.3, 131.8, 129.1, 128.8, 128.4, 126.1, 125.5, 123.8, 91.5, 89.6, 30.0 ppm. **MS(ASAP):** *m/z* 559.092 [M+H]⁺, **Acc-MS (ASAP⁺):** *m/z* 559.0853[M+H]⁺, calcd. for C₃₄H₂₃O₂S₃ *m/z* 559.086 (|Δ*m/z*| = 1.3 ppm), **Anal. Calc.** for C₃₄H₂₂O₂S₃: C, 73.09; H, 3.97%. **Found:** C, 72.82; H, 3.83 %.

S2. NMR spectra of reported compounds

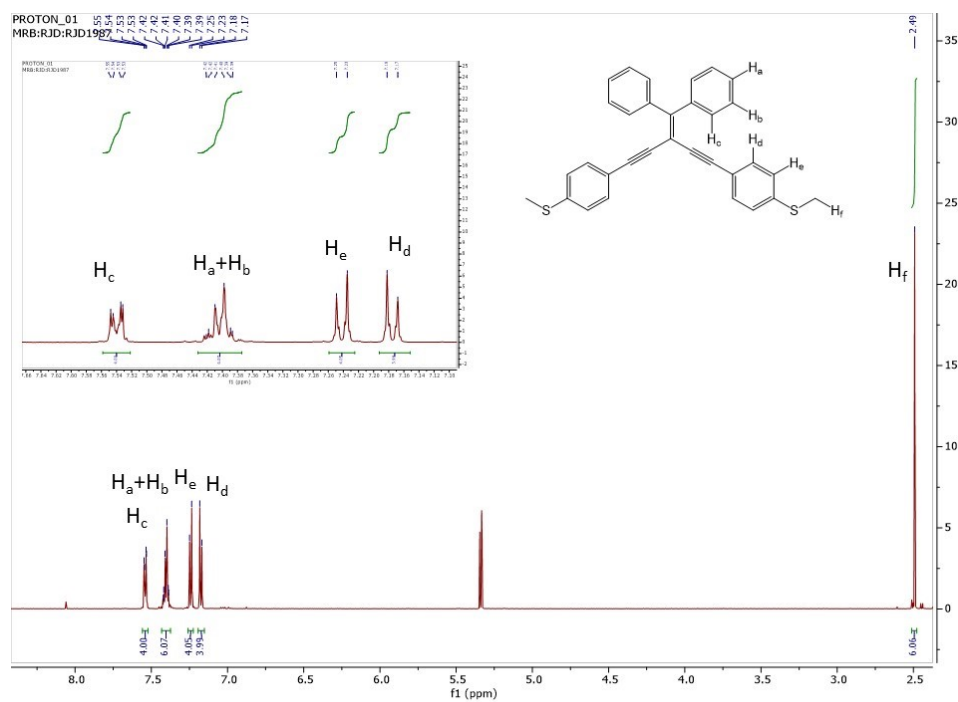


Fig. S1 $^1\text{H-NMR}$ spectrum of **1a** recorded in CD_2Cl_2 .

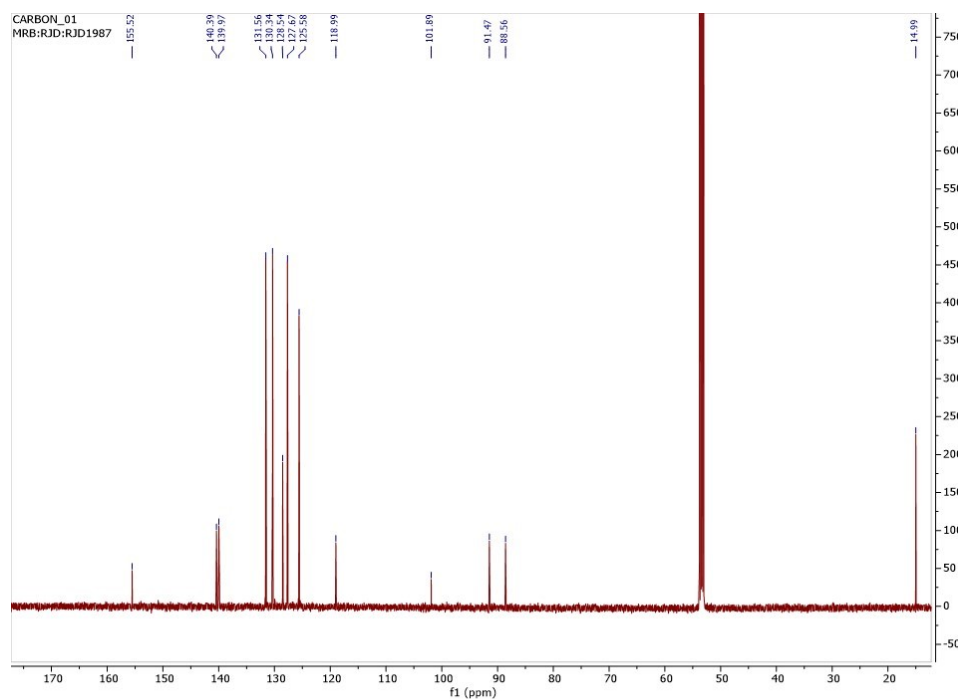


Fig. S2 $^{13}\text{C-NMR}$ spectrum of **1a** recorded in CD_2Cl_2 .

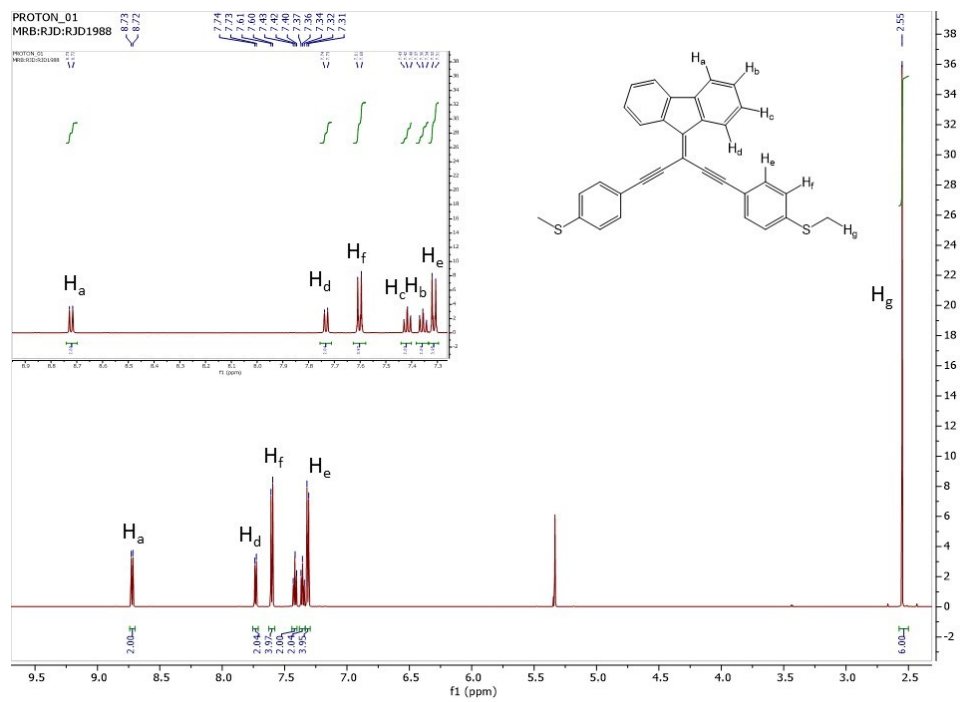


Fig. S3 ^1H -NMR spectrum of **2a** recorded in CD_2Cl_2 .

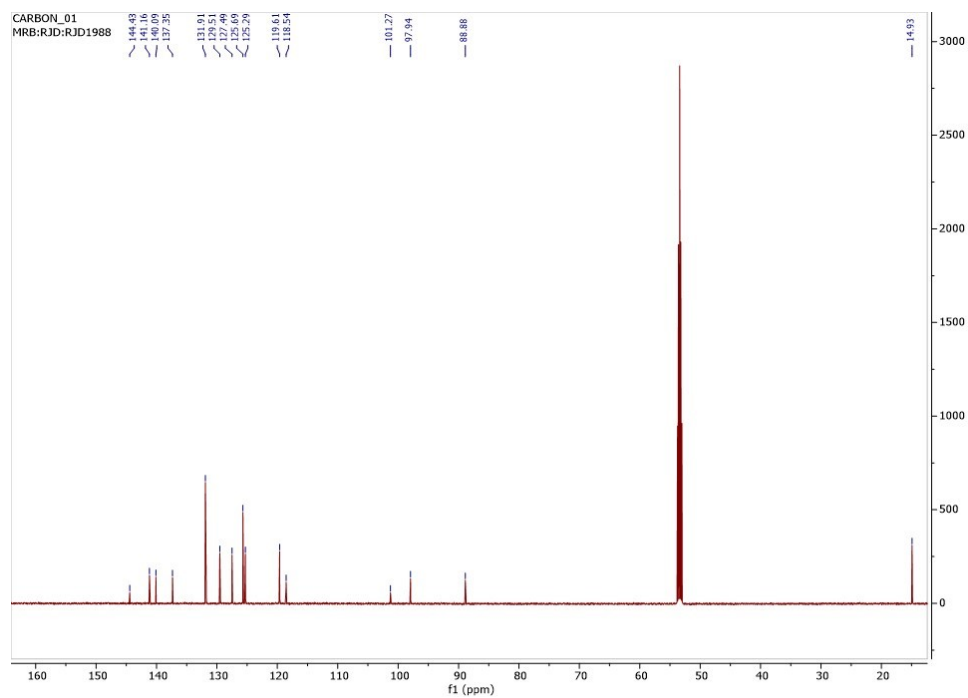


Fig. S4 ^{13}C -NMR spectrum of **2a** recorded in CD_2Cl_2 .

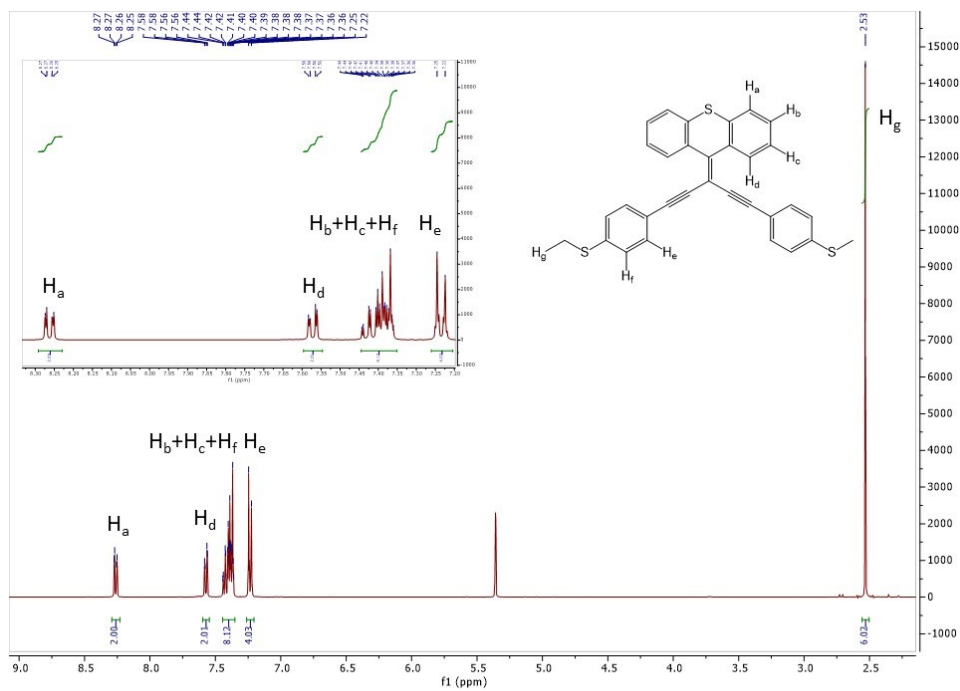


Fig. S5 1H -NMR spectrum of **3a** recorded in CD_2Cl_2 .

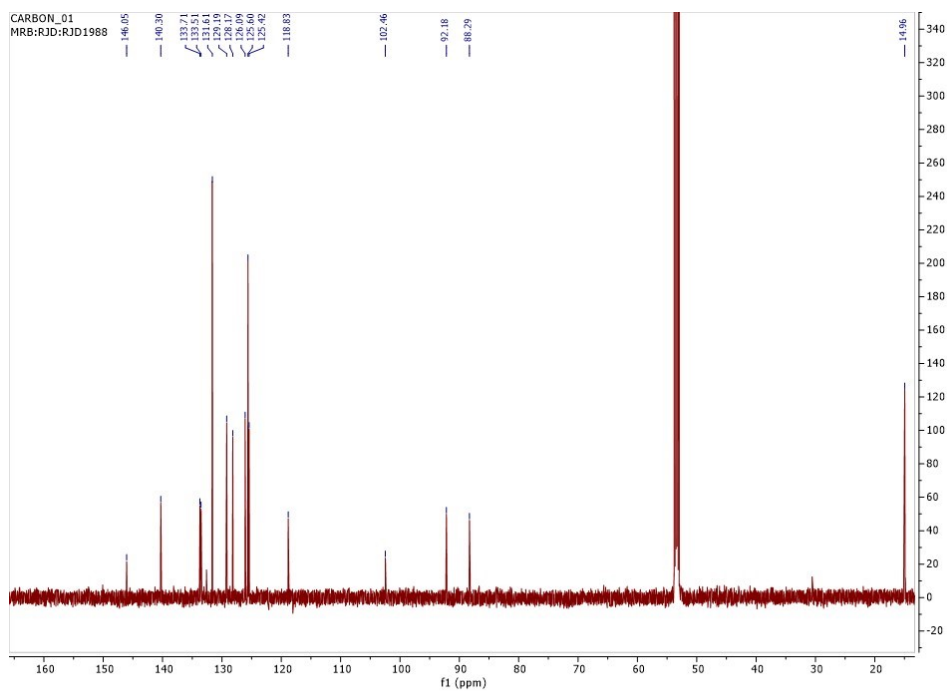


Fig. S6 ^{13}C -NMR spectrum of **3a** recorded in CD_2Cl_2 .

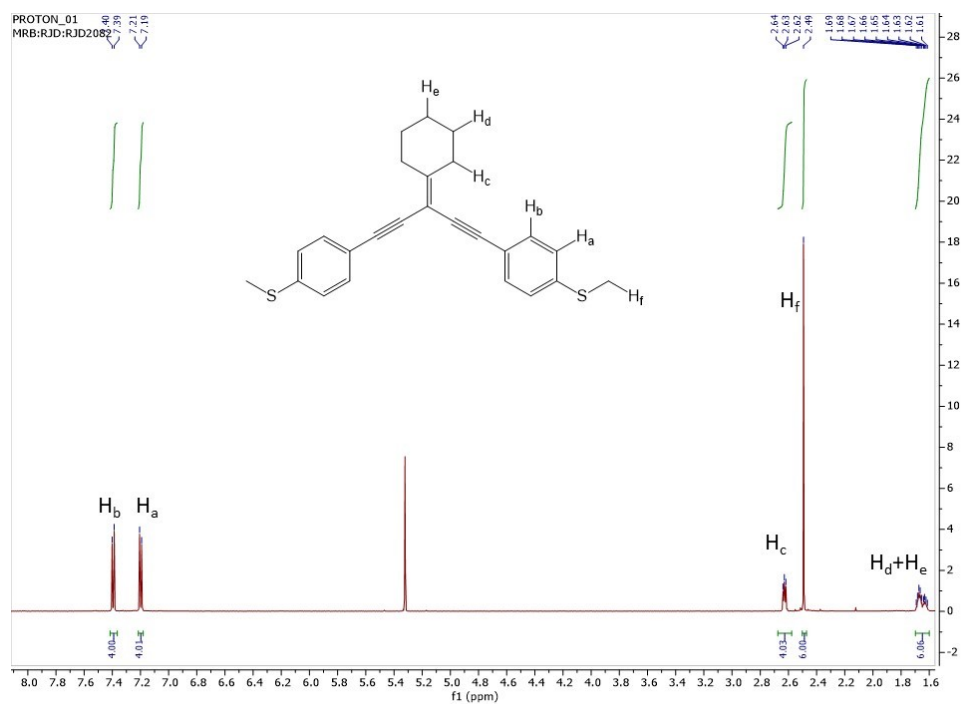


Fig. S7 ^1H -NMR spectrum of **4** recorded in CD_2Cl_2 .

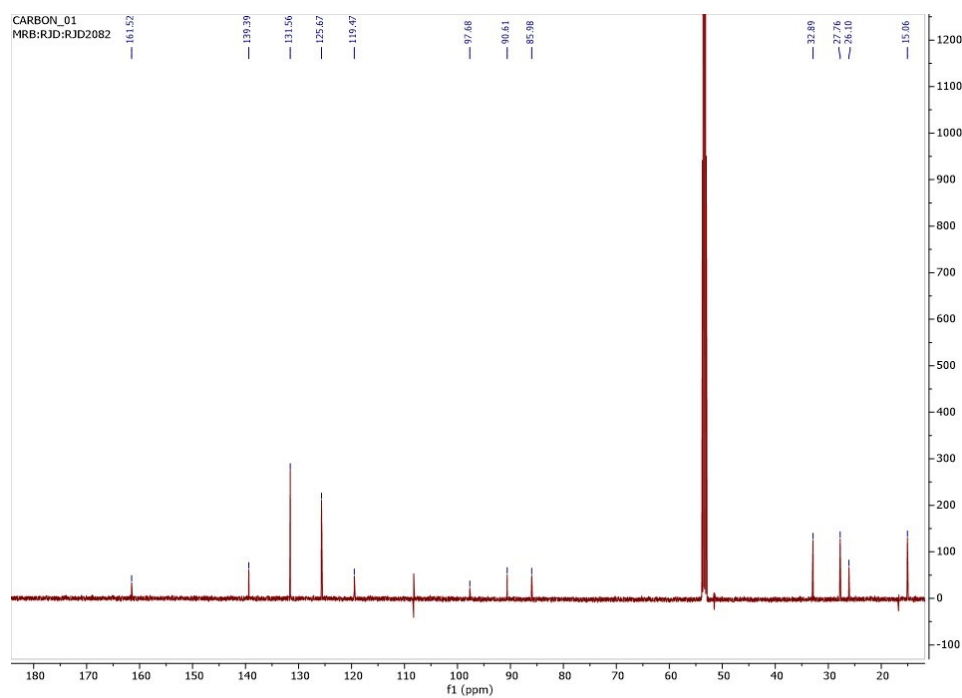


Fig. S8 ^{13}C -NMR spectrum of **4** recorded in CD_2Cl_2 .

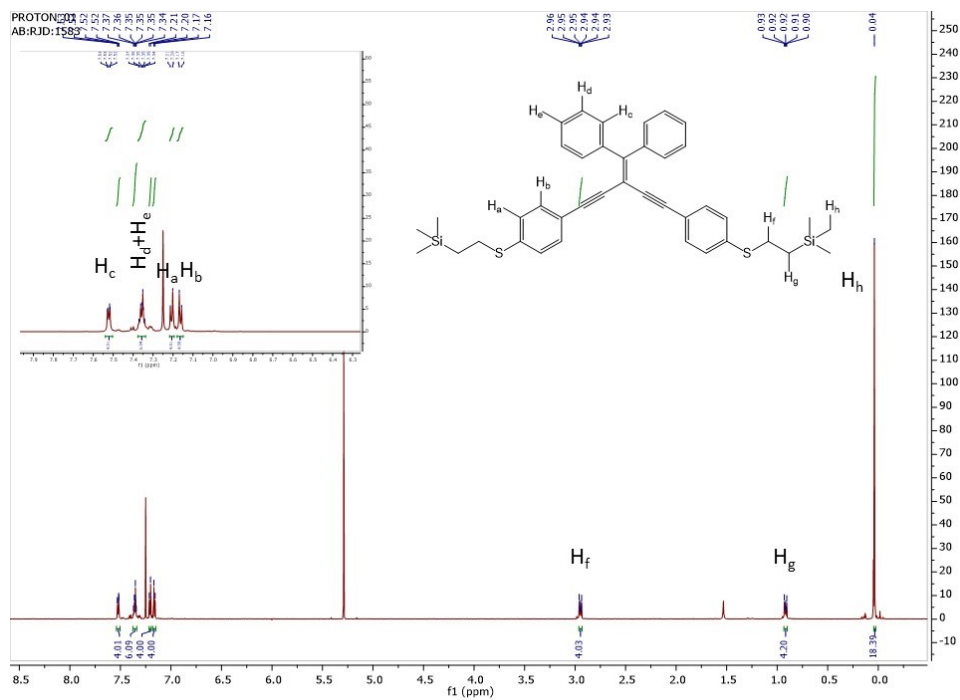


Fig. S9 ¹H-NMR spectrum of Ph₂-STMS₂ recorded in CDCl₃.

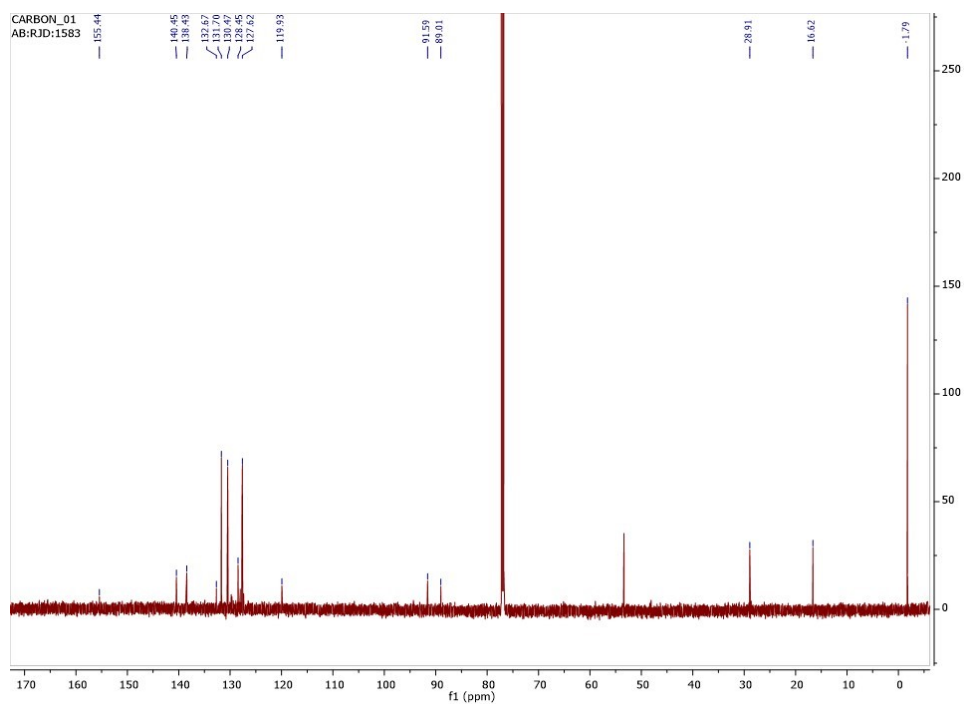


Fig. S10 ¹³C-NMR spectrum of Ph₂-STMS₂ recorded in CDCl₃.

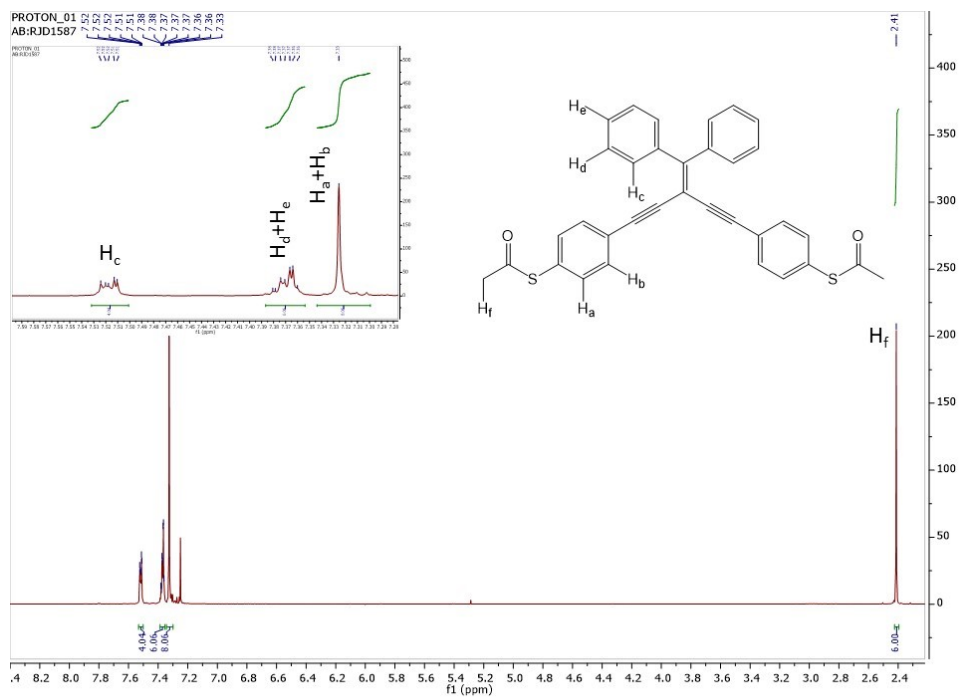


Fig. S11 ¹H-NMR spectrum of **1b** recorded in CDCl₃.

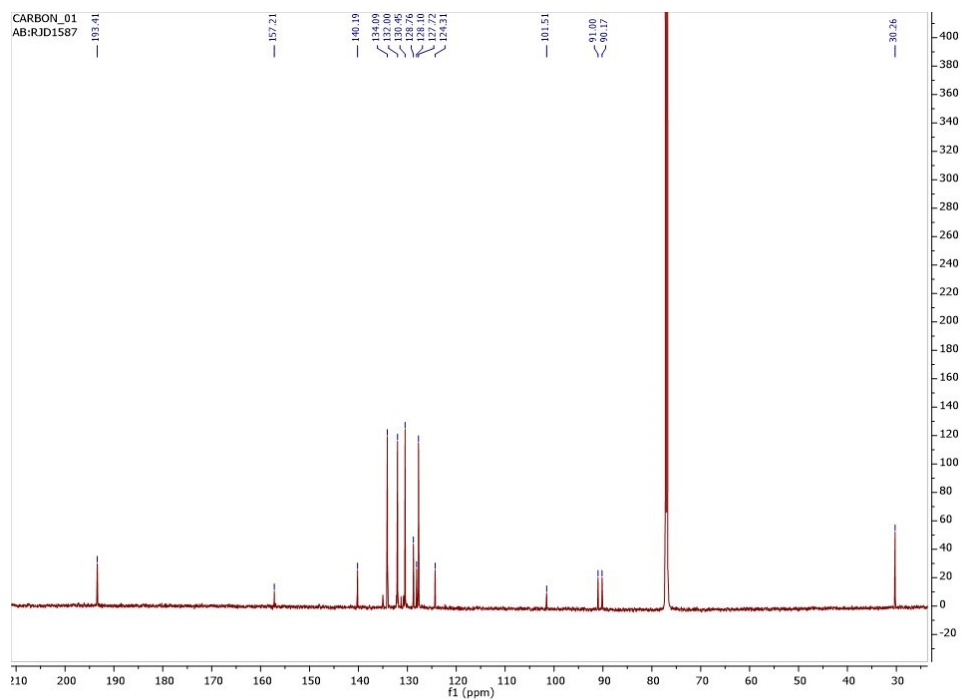


Fig. S12 ¹³C-NMR spectrum of **1b** recorded in CDCl₃.

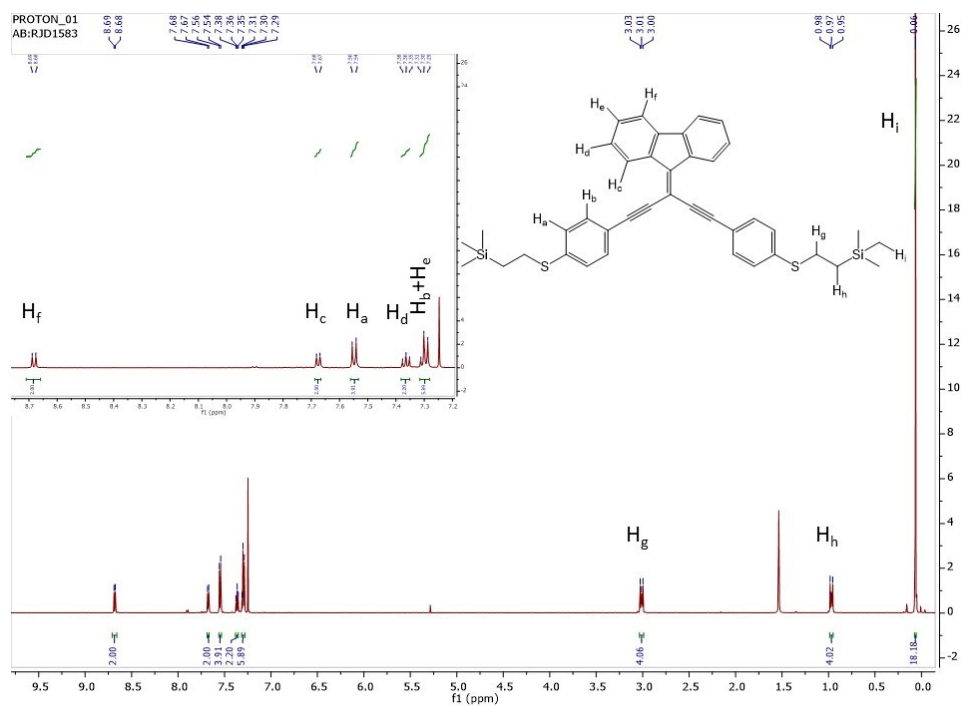


Fig. S13 ^1H -NMR spectrum of **Fluorene-STMS₂** recorded in CDCl_3 .

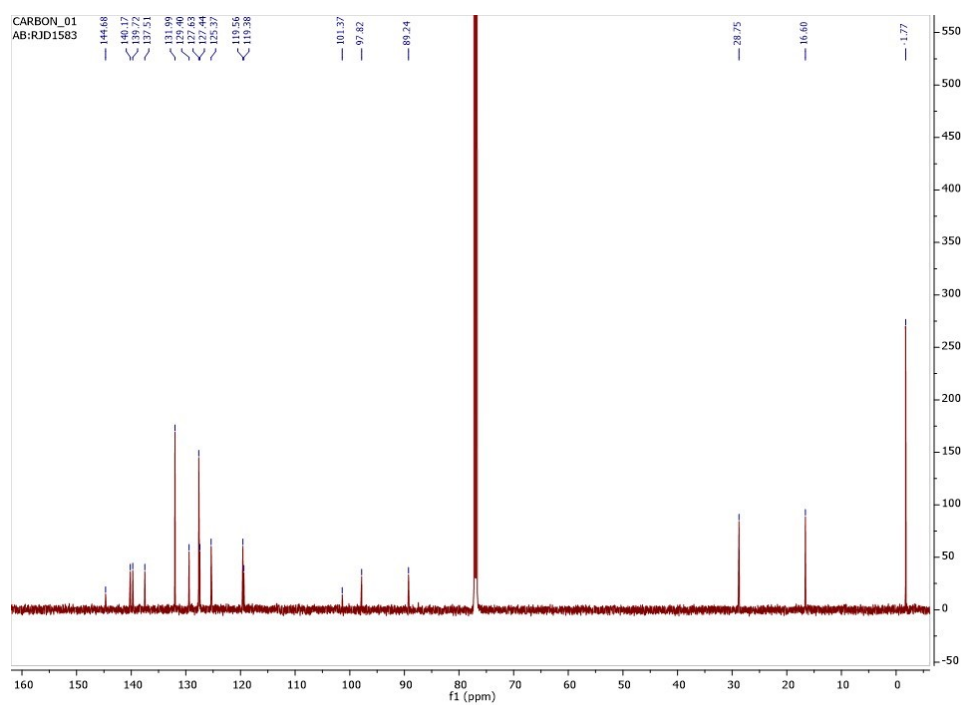


Fig. S14 ^{13}C -NMR spectrum of **Fluorene-STMS₂** recorded in CDCl_3 .

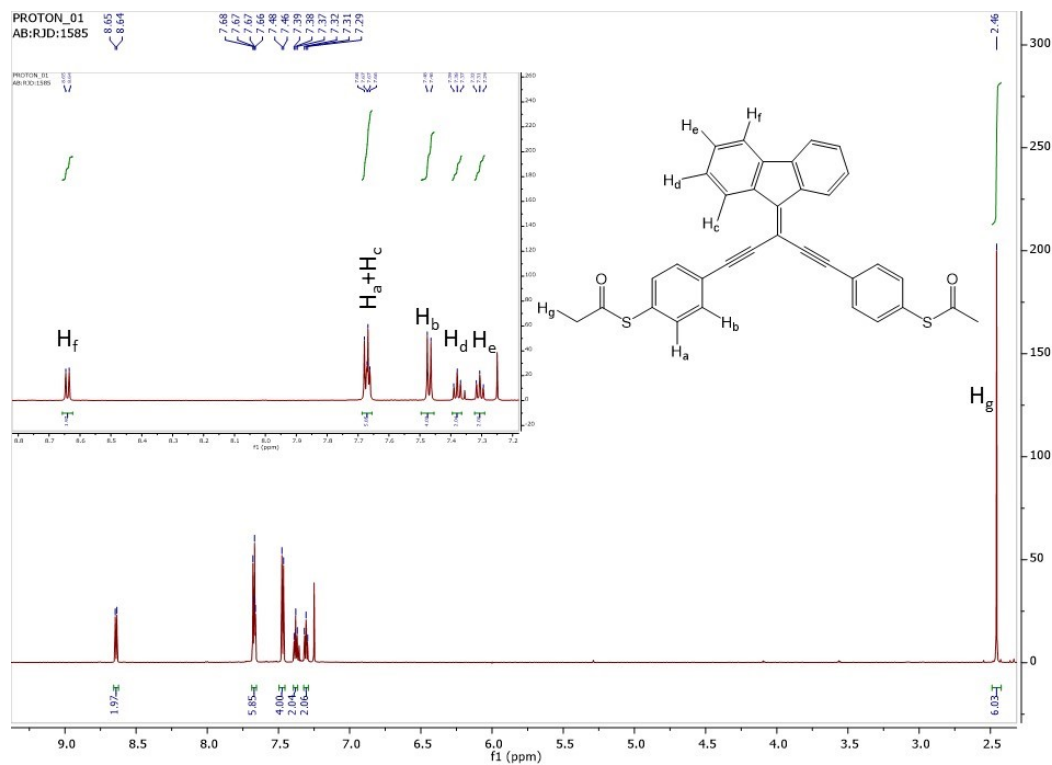


Fig. S15 $^1\text{H-NMR}$ spectrum of **2b** recorded in CDCl_3 .



Fig. S16 $^{13}\text{C-NMR}$ spectrum of **2b** recorded in CDCl_3 .

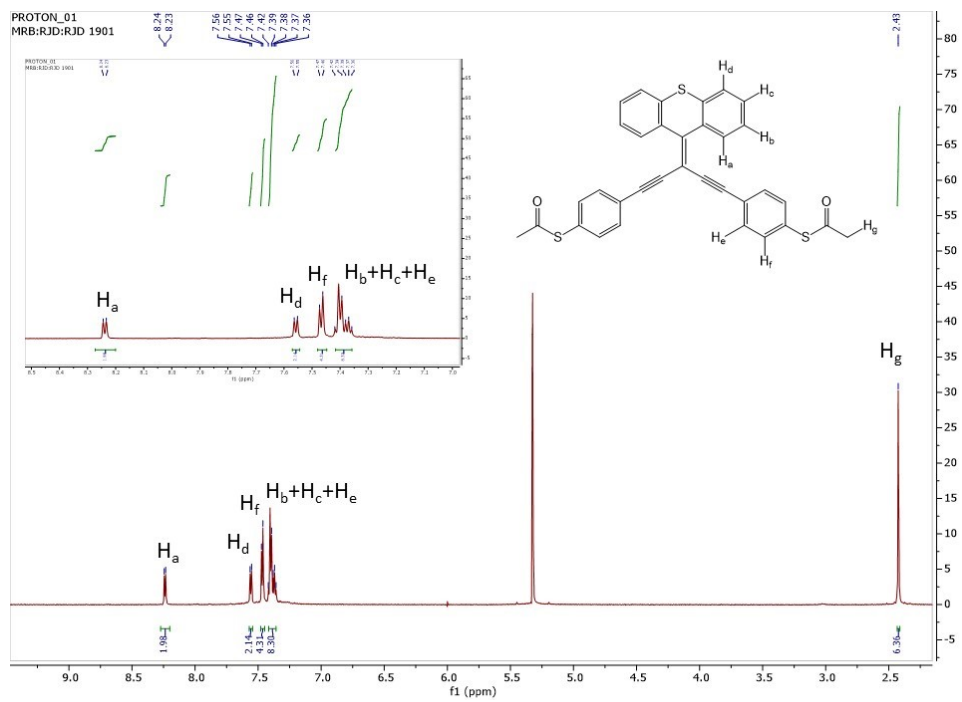


Fig. S17 ^1H -NMR spectrum of **3b** recorded in CD_2Cl_2 .

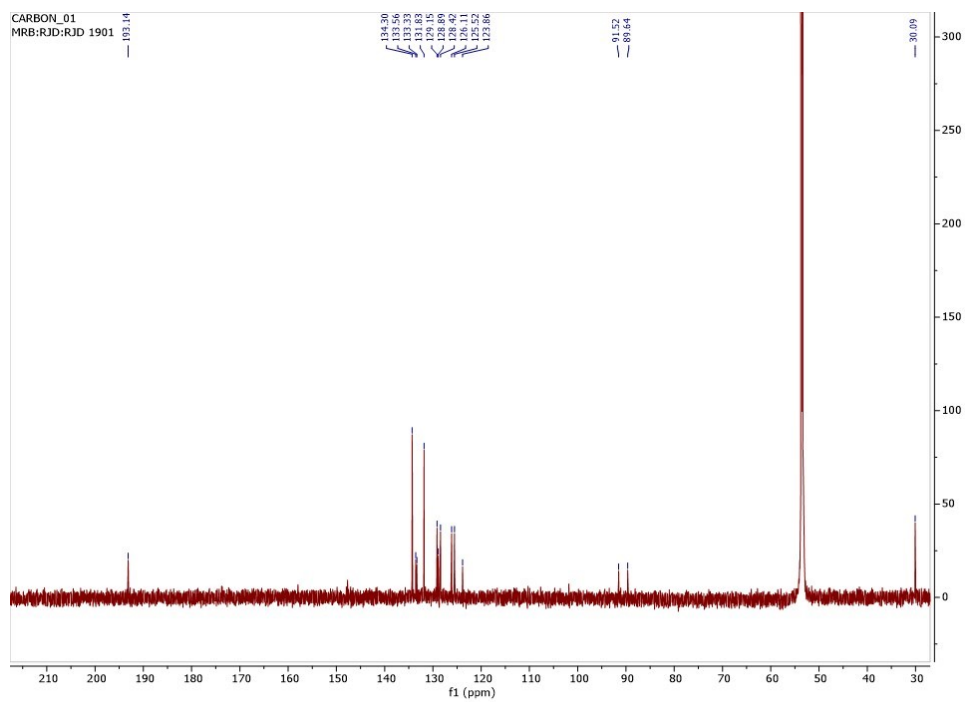


Fig. S18 ^{13}C -NMR spectrum of **3b** recorded in CD_2Cl_2 .

S3. Crystallographic data

Single-crystals of **2a** were grown by diffusion of *n*-pentane vapour into a solution of **2a** in THF. The X-ray diffraction experiment was carried out on a Bruker D8 Venture 3-circle diffractometer, equipped with PHOTON III C14 MM CPAD area detector, using Mo- $K\alpha$ radiation ($\lambda=0.71073$ Å) from Incoatec I μ S 3.00 microsource with focusing mirrors and were cooled Cryostream 700 (Oxford Cryosystems) open-flow N₂ gas cryostat. The data were collected in shutterless mode by narrow frame ω scans covering full sphere of reciprocal space, using APEX3 v. 2019.1-0 software, reflection intensities integrated using SAINT v. 8.40A software (Bruker AXS, 2019). Data were corrected for absorption by semi-empirical method based on Laue equivalents and multiple scans, using SADABS v. 2016/2 software⁶. The structure was solved by dual-space intrinsic phasing method using SHELXT 2018/2 program⁷ and refined by full-matrix least squares using SHELXL 2018/3 software⁷ on OLEX2 platform⁸. The crystal was an inversion twin with 0.6(1):0.4(1) component ratio. *Crystal data*: C₃₂H₂₂S₂, *M*=470.61, *T*=120 K, monoclinic, space group *Cc* (No. 9), *a*=36.920(3), *b*=9.3237(8), *c*=27.635(2) Å, β =101.301(3)°, *V*=9328(2) Å³, *Z*=16, *D*_c=1.340 g cm⁻³, μ =0.25 mm⁻¹, 42858 reflections with $2\theta \leq 50^\circ$, 16359 unique, *R*_{int}=0.073, final *R*(*F*)=0.061 on 11423 reflections with $I \geq 2\sigma(I)$, *wR*(*F*²)=0.135 on all data. Full crystallographic information (including structure factors) in CIF format has been deposited with Cambridge Crystallographic Data Centre, CCDC-2141972.

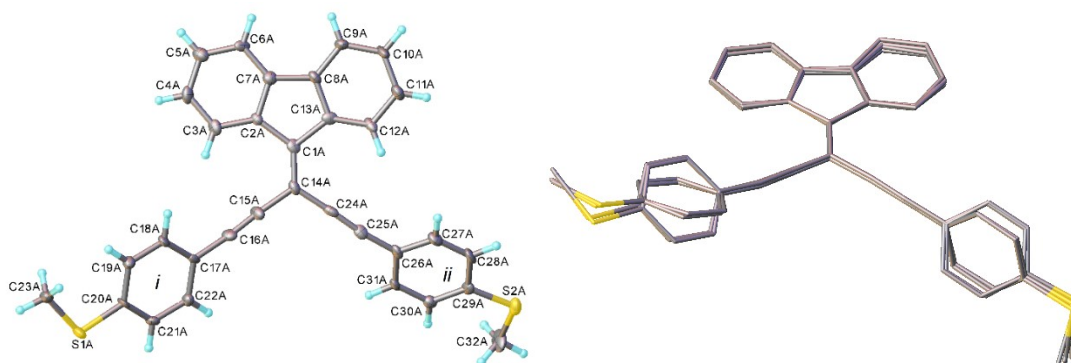


Fig. S19 Left: X-ray molecular structure of independent molecule A; right: overlay of molecules A-D with hydrogen atoms omitted.

A single-crystal X-ray diffraction study of **2a** revealed four molecules per asymmetric unit, each showing a different conformation resulting from the thioanisole; an overlay of molecules A-D is provided in Fig. 19 to highlight their difference. In each case, the planar fluorene moiety is co-planar with the ethylene bond within 1.1(6) to 5.1(6)°. The twists about this bond (6.4(4) to 6.9(5)°) and the deviations of acetylenic fragments from linearity (5.4 to 11.0°) are similar. However, the dihedral angles between the fluorene moiety and thioanisole rings vary widely, both within and between molecules (22.1(2) to 88.4(2)°), as governed by the packing interactions, which accords with the typical low rotational energy barrier around the alkyne axis of phenylacetylene derivatives⁹. Nevertheless, all S–Me bonds are nearly co-planar with the corresponding arene rings, within 3.2(5) to 10.8(4)°. There are no π - π stacking interactions in the structure, in contrast with 9-methylene-10,10-bis(phenylethynyl)fluorene and its bis(3,5-bis(trifluoromethyl)phenyl) analogue¹⁰, where approximately planar molecules (with fluorene/phenyl dihedral angles of 4.0–14.8° and 5.4°, respectively) form infinite stacks.

Table S1 Selected bond distances (Å) and angles (°) for **2a**

Molecule	A	B	C	D
C(1)-C(14)	1.348(12)	1.355(12)	1.374(12)	1.362(12)
C(14)-C(15)	1.478(11)	1.452(11)	1.457(13)	1.437(12)
C(15)-C(16)	1.179(12)	1.189(12)	1.172(13)	1.195(12)
C(16)-C(17)	1.440(12)	1.446(12)	1.466(13)	1.430(12)
C(14)-C(24)	1.417(14)	1.417(14)	1.410(11)	1.457(14)
C(24)-C(25)	1.219(14)	1.230(14)	1.201(12)	1.176(14)
C(25)-C(26)	1.410(14)	1.412(14)	1.436(11)	1.461(13)
C(20)-S(1)	1.769(8)	1.767(8)	1.767(10)	1.773(9)
C(29)-S(2)	1.763(10)	1.760(10)	1.765(8)	1.770(10)
C(14)-C(15)-C(16)	174.9(11)	175.5(11)	175.4(10)	174.9(10)
C(15)-C(16)-C(17)	174.9(10)	173.5(10)	174.6(10)	171.5(10)
C(14)-C(24)-C(25)	176.1(10)	176.4(10)	174.4(10)	176.9(11)
C(24)-C(25)-C(26)	171.1(11)	174.1(10)	171.6(10)	177.4(11)
Fluorene/arene(i) interplanar angle	34.1(2)	22.1(2)	48.1(2)	29.6(2)
Fluorene/arene(ii) interplanar angle	40.8(2)	88.4(2)	36.3(2)	81.6(2)
Fluorene/ethylene bond tilt angle	1.1(6)	5.1(6)	4.8(6)	1.3(6)
Torsion around ethylene bond	6.9(5)	6.5(4)	6.4(4)	6.7(4)
Torsion around C(20)-S(1) bond	7.3(4)	3.2(5)	8.1(4)	3.8(4)
Torsion around C(29)-S(2) bond	8.1(5)	9.8(4)	7.4(4)	10.8(4)

S4. Photophysical Measurements

UV-Visible absorption spectra were recorded at room-temperature using a UV-Visible spectrophotometer Evolution 220 from Thermo Scientific in quartz cuvettes with path length $l = 1$ cm.

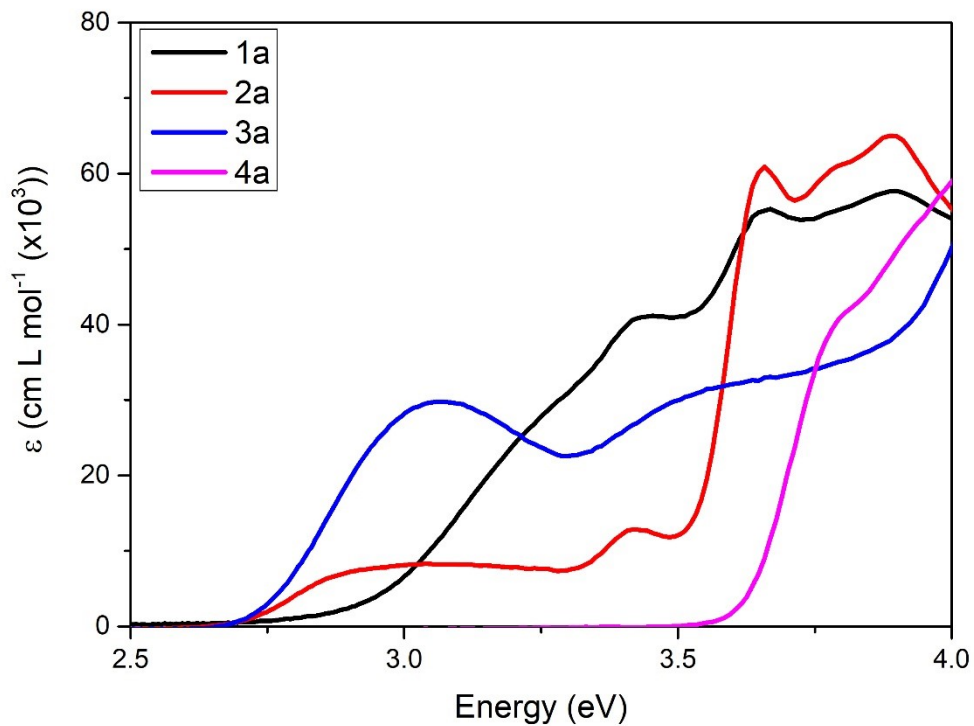


Fig. S20 UV-Visible absorption spectra for compounds **1-3a**, and **4** recorded in DCM.

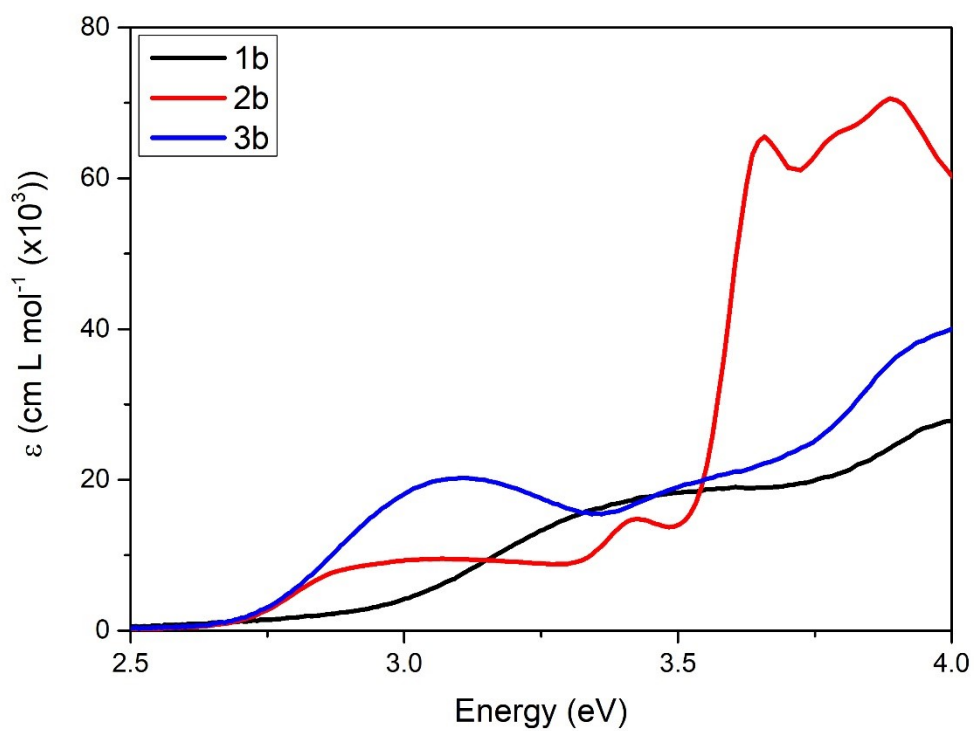


Fig. S21 UV-Visible absorption spectra for compounds **1-3b** recorded in DCM.

Table S2 ΔE |HOMO-LUMO| determined by UV-Visible absorption spectra.

Compound	ΔE HOMO-LUMO (eV)
1a	2.93
2a	2.70
3a	2.75
4	3.63
1b	2.91
2b	2.71
3c	2.72

S5. Conductance Measurements

All compounds were deposited onto Au(111) samples using the drop casting technique. Au samples were annealed at approximately 900 K for 1-2 minutes, allowed to cool down to room temperature and then introduced into a 1 mM dichloromethane (DCM) solution of the corresponding molecule. After 40 minutes samples were dried off with nitrogen gas to eliminate possible molecular clusters on the surface. Mechanically cut Au wires (0.25 mm diameter, 99.99% purity, Goodfellow) were used as STM tips. A bias voltage was applied to the sample, using $V_{bias} = 100 \text{ mV}$. The tunnelling current was amplified using a double-stage, home-made, linear current-voltage (I - V)-converter with an overall gain of $2.5 \times 10^{10} \text{ V/A}$ ($5 \times 10^8 \text{ V/A}$ in the first stage and multiplied by a factor of 50 in the second one).

The clustering analysis applied was based on the k-means algorithm supported by Matlab. To transform the I Z traces into valid inputs for the algorithm, we assigned a Lorentzian distribution to each conductance point and then we summed all of them. The number of clusters was initially chosen to be 2 and was then successively increased until the complete conductance distribution was properly fitted, without major overlapping between the conductance clusters. With this technique traces with or without a molecular plateau were separated and also traces with different conductance plateaus could be separated into different clusters for each set of measurements.

Fig. S22 and Fig. S23 shows 2D conductance vs distance histograms of compounds **1a-3a** and **1b-3b**, respectively, with their respective clusters with individual I Z traces of each one in black.

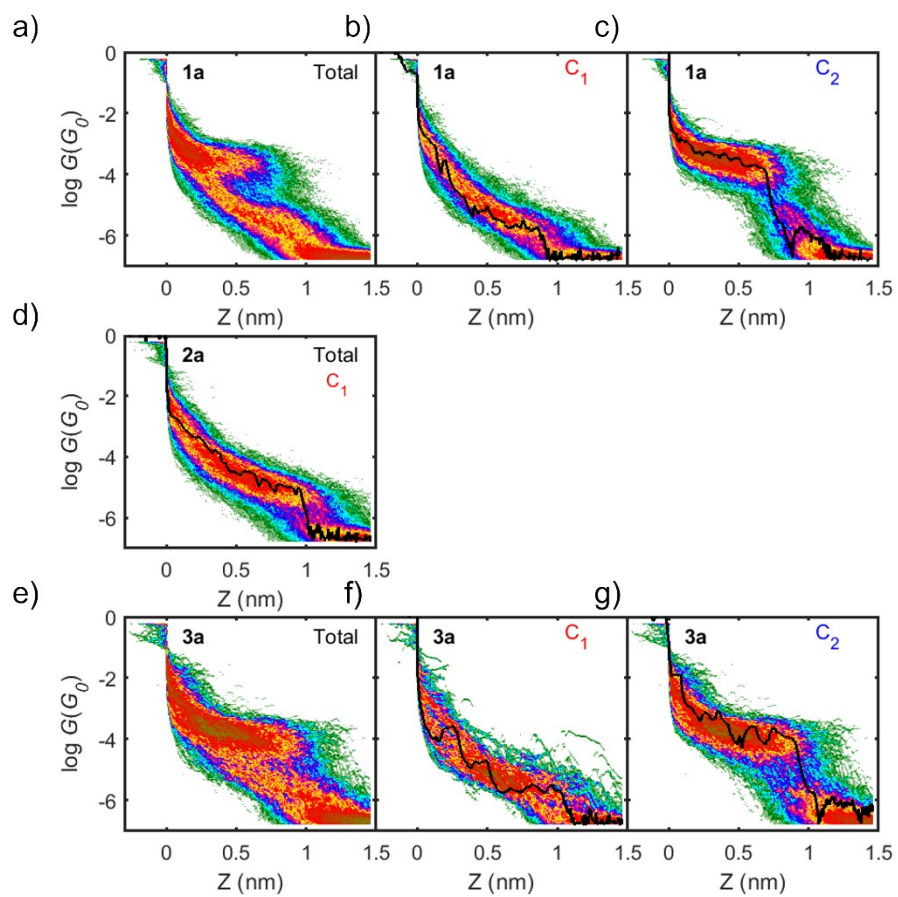


Fig. S22 2D conductance vs distance histograms of compounds **1a-3a** and their respective clusters C_1 and C_2 with individual examples of IZ traces for each cluster.

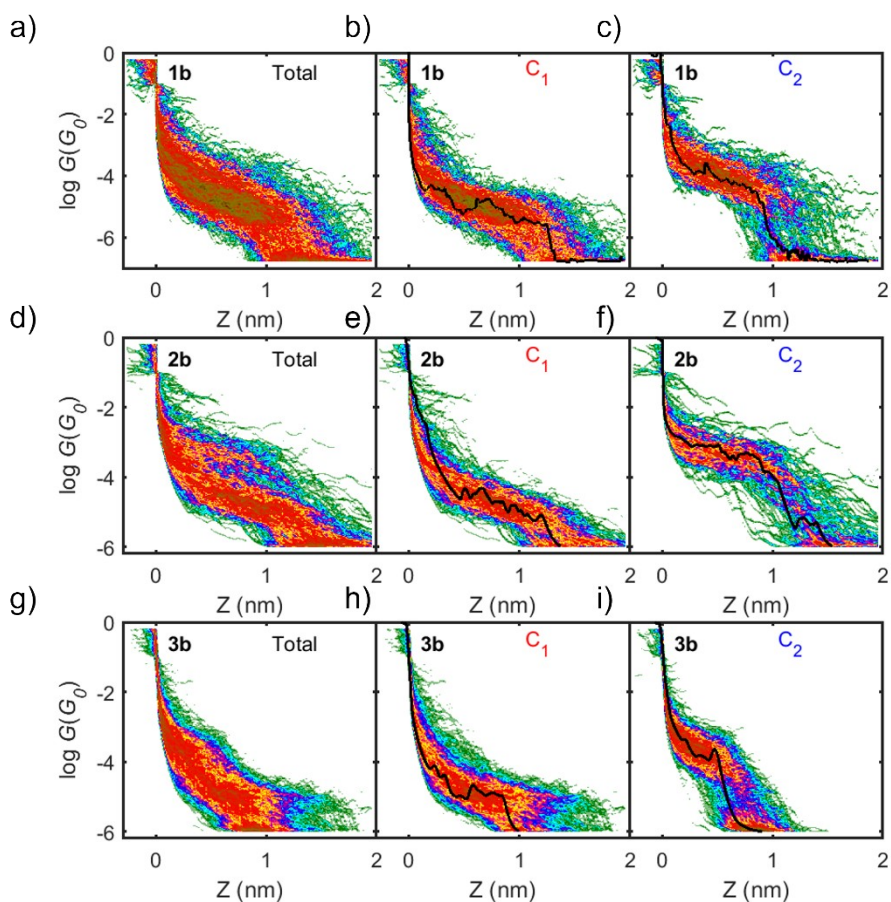


Fig. S23 2D conductance vs distance histograms of compounds **1b-3b** and their respective clusters C_1 and C_2 with individual examples of IZ traces for each cluster.

The apparent stretching length (L_s) of the molecular plateaus were obtained by fitting a Gaussian distribution to each conductance peak and obtaining the length differences between $\bar{G}_{1,2} \pm \sigma_{1,2}$, where $\bar{G}_{1,2}$ and $\sigma_{1,2}$ are the mean conductance value and the standard deviation of the Gaussian fitting curves, respectively. In order to take into account the multiple junction configurations, the Gaussian distributions were fitted to all the distances obtained and the 90% decay distance of the Gaussian fit was then calculated¹¹. The values are gathered in Table S3.

Table S3 Mean conductance values $\bar{G}_{1,2}$ and apparent stretching lengths L_s of clusters C_1 and C_2 for all compounds, measured at $V_{bias} = 100$ mV.

		1a	1b	2a	2b	3a	3b
C_1	$\bar{G}_1 \log G(G_0)$	-5.3	-4.9	-4.9	-4.9	-5.3	-4.9
	L_s (nm)	1.2	1.6	1.3	1.8	1.4	1.5
C_2	$\bar{G}_2 \log G(G_0)$	-3.5	-3.7	-	-3.5	-3.7	-3.5
	L_s (nm)	1.0	1.1	-	1.4	1.2	0.9

The conductance of compound **4a** was also measured with $V_{bias} = 600$ mV to explore a larger conductance range. Fig. S24a shows the corresponding 1D conductance histogram (solid line) and the fitted Gaussian distribution to the conductance peak (dotted line) whose mean value is given as \bar{G}_1 in the figure, and Fig. S24b shows the 2D conductance vs distance histogram of compound **4a**.

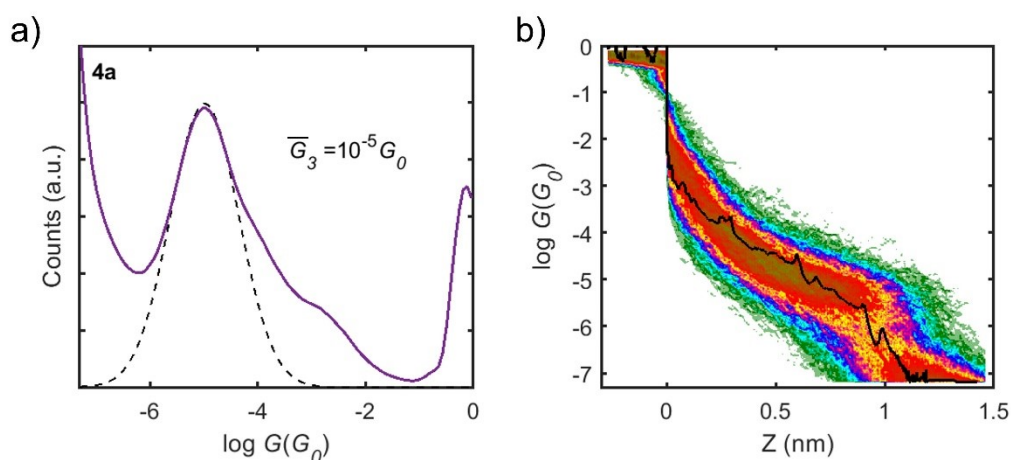


Fig. S24 (a) 1D conductance histogram of compound **4**. Conductance mean value (\bar{G}_1) of the Gaussian fit to the conductance peak (dashed line) is also included. (b) 2D conductance vs distance histogram of compound **4**.

Conductance measurements for all compounds with $V_{bias} = 600$ mV were carried out to explore other possible molecular configurations inside the junction. Using again the

clustering technique we were able to distinguish a third cluster (C_3) in a lower conductance range for all the molecules **1b-3b** with S anchor groups. Individual conductance vs distance traces of C_3 are shown in Figure S23b,d,f) and 1D histograms are shown in Figure S23a,c,e) in green and their respective Gaussian fits to each conductance peak, are shown as black dotted lines. The apparent stretching length of all the peaks obtained with $V_{bias} = 600$ mV are gathered in Table S4.2.

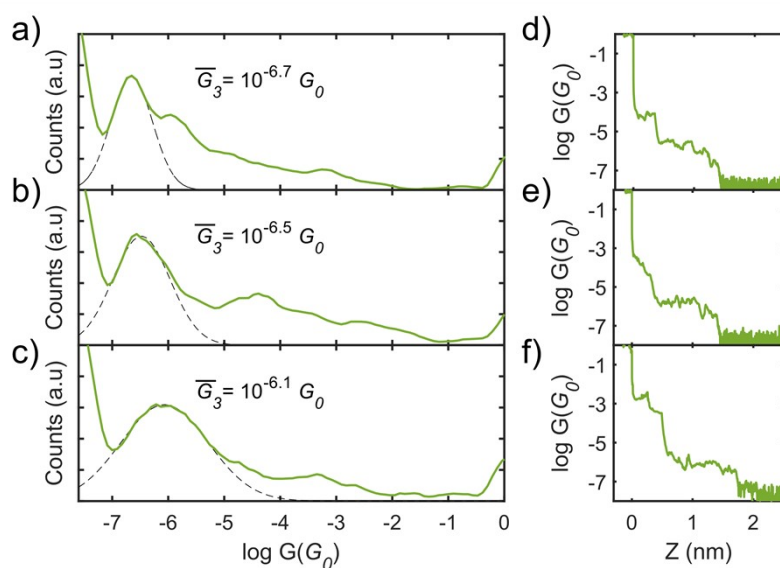


Fig. S25 (a-c) 1D conductance histograms of the third conductance plateau for **1-3b**

compounds at $V_{bias} = 600$ mV. \bar{G}_3 values are obtained from the mean value of a Gaussian fit to the conductance peak (black dashed lines). (d-f) Individual conductance vs distance traces of C_3 for **1-3b** compounds at $V_{bias} = 600$ mV.

Table S4 Mean conductance values $\overline{G}_{1,2,3}$ and apparent stretching lengths L_s of each cluster for all compounds, measured at $V_{bias} = 600$ mV.

		1a	1b	2a	2b	3a	3b
C₁	$\overline{G}_1 \log G(G_0)$	-5.4	-4.6	-5.0	-4.7	-5.0	-4.9
	L_s (nm)	1.5	1.7	1.3	1.9	1.5	1.9
C₂	$\overline{G}_2 \log G(G_0)$	-3.4	-3.3	-	-3.2	-3.6	-3.2
	L_s (nm)	1.1	1.1	-	1.5	1.2	1.1
C₃	$\overline{G}_3 \log G(G_0)$	-	-6	-	-6.4	-	-6.6
	L_s (nm)	-	1.9	-	2.5	-	1.9

Comparing the results shown in Table S4 with the theoretical calculations of the molecular junctions with a theta angle close to 0, we assign this cluster C3 to a configuration where the pendant groups of the molecules are not interacting with the electrodes, leading into a lower conductance values and larger apparent stretching lengths.

S6. Seebeck Coefficient Measurements

To perform Seebeck coefficient measurements a home-built STM was used, capable of measuring simultaneously the conductance (G) and the thermovoltage (V_{th}) of the molecular junctions formed. The tip was heated using a $1\text{ K}\Omega$ surface resistor, creating a temperature difference (ΔT) between the tip and the sample, with the tip at $T_h > T_{ambient}$ and the sample at $T_c = T_{ambient}$. This temperature difference not only generates a V_{th} in the molecular junction but also in the copper lead that connects the tip to the rest of the setup. Considering all these factors the thermo-electric equation of the circuit can be expressed as:

$$I = G(V_{bias} + V_{th}) = G(V_{bias} + S\Delta T - S_{lead}\Delta T), \quad (1)$$

where S and S_{lead} are the Seebeck coefficients of the molecule and the copper lead, respectively. Figure S24a shows a scheme of the equivalent electrical-thermal circuit of the STM.

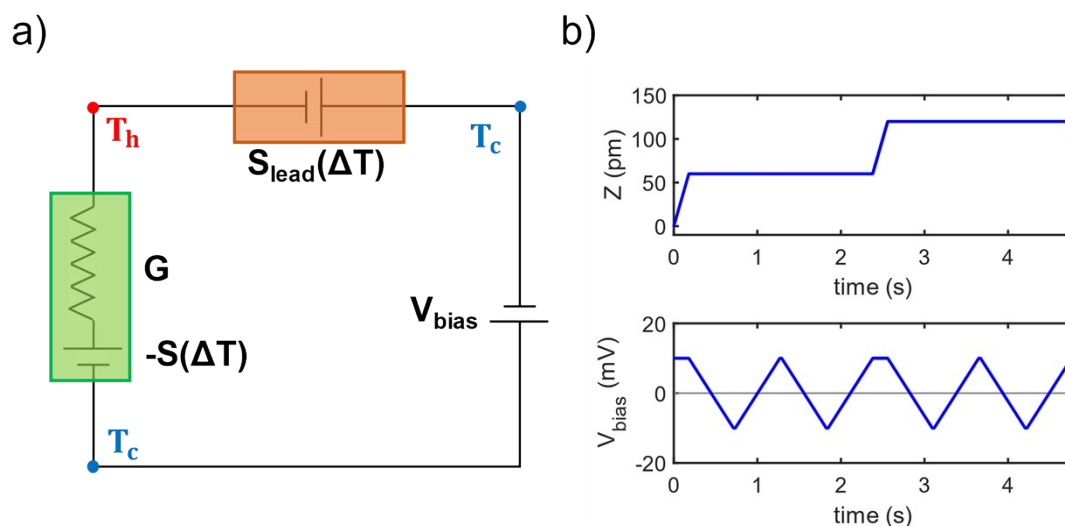


Fig. S26 (a) Scheme of the electrical-thermal circuit of the STM, where V_{bias} is the bias voltage applied; S and S_{lead} are the Seebeck coefficients of the molecule and the copper lead, respectively; G is the conductance of the molecular junction, and ΔT is the temperature

difference between the tip (at $T_h > T_c$) and the sample ($T_c = T_{ambient}$), and (b-c). Tip displacement Z and V_{bias} signals, respectively, during a thermovoltage measurement. While the molecular junction is formed, the tip displacement is momentarily stopped and the V_{bias} is ramped between ± 10 mV.

In order to get a better stability of the junction, the V_{bias} was fixed at 10 mV, avoiding large voltage changes. While forming the molecular junctions, small IV curves of ± 10 mV are acquired to perform the thermoelectric characterization. An example of the tip displacement Z and the bias voltage V_{bias} signals applied in this case are shown in Figure S24b-c, respectively. The tip displacement is momentarily stopped during the junction formation and the small IV curves are measured. Applying equation (1), V_{th} and G are simultaneously obtained from the zero-current crossing point and the slope of the IV curves, respectively, and the Seebeck coefficient is then given by $S = -V_{th}/\Delta T$. Multiple sets of V_{th} data were measured for different ΔT values at different days and combined all together in order to obtain more statistically robust results. For consistency, applying the above-mentioned clustering technique we separate the measured V_{th} values into clusters C_1 and C_2 , based on the IZ traces. The Seebeck coefficient of each cluster is then obtained from the slope of the linear regression of all V_{th} vs ΔT points.

b) Theoretical

S7. Theoretical Methods

The optimum geometry of each of the molecules was calculated using the density functional code SIESTA. These used a double-zeta polarized (DZP) basis set defined by a confining cut-off of 0.008 Rydbergs, norm conserving pseudopotentials, an energy cut-off of 150 Rydbergs and the generalised gradient approximation (GGA) method to describe the exchange correlation functional. All forces on the atoms were relaxed to a force tolerance of 0.01 eV/Å. The molecule was then contacted to gold electrodes to form the molecular junction. The binding geometry was found by calculating the optimum binding energy as described in Section S10. The gold electrodes were modelled as 6 layers of (111) gold each containing 54 atoms, a double-zeta basis was used to describe the gold atoms and a Hamiltonian describing this extended molecule was extracted using SIESTA. The zero bias transmission coefficient $T(E)$, conductance G and the Seebeck coefficient S were calculated using the quantum transport code Gollum.

S8. Molecular Orbitals

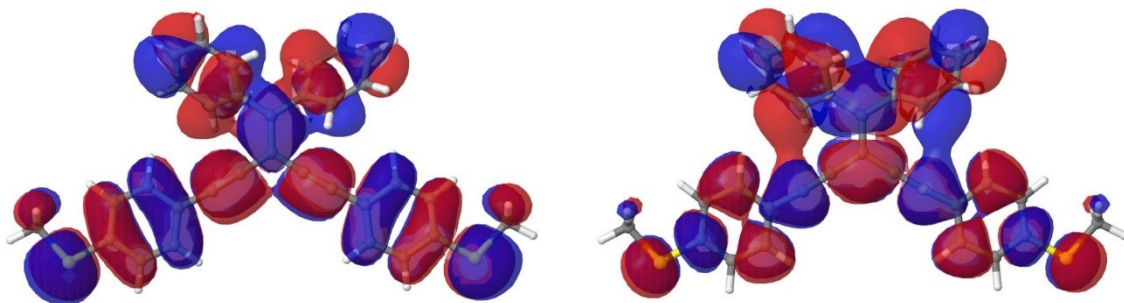


Fig. S27 HOMO (left) and LUMO (right) orbitals of molecule **1a**.

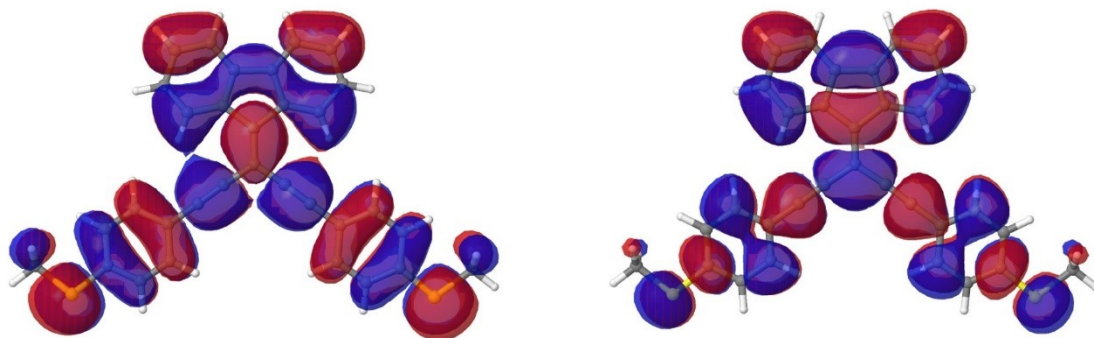


Fig. S28 HOMO (left) and LUMO (right) orbitals of molecule **2a**.

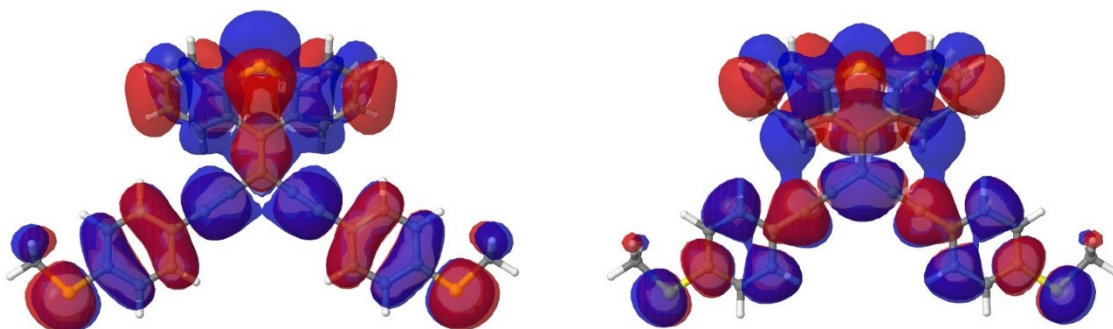


Fig. S29 HOMO (left) and LUMO (right) orbitals of molecule **3a**.

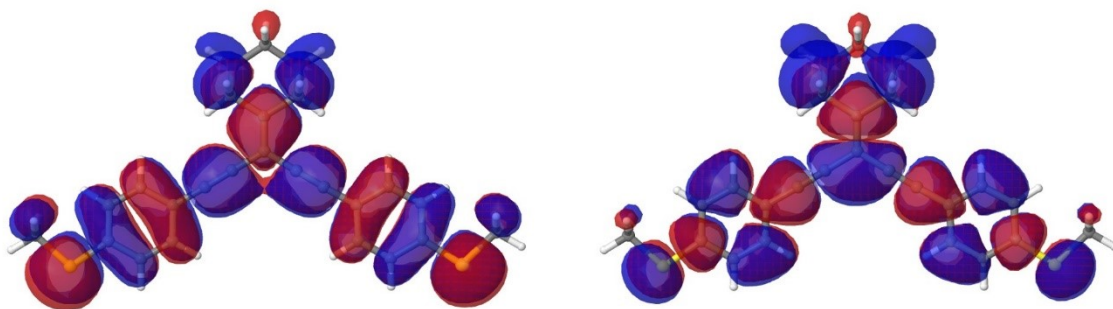


Fig. S30 HOMO (left) and LUMO (right) orbitals of molecule **4**.

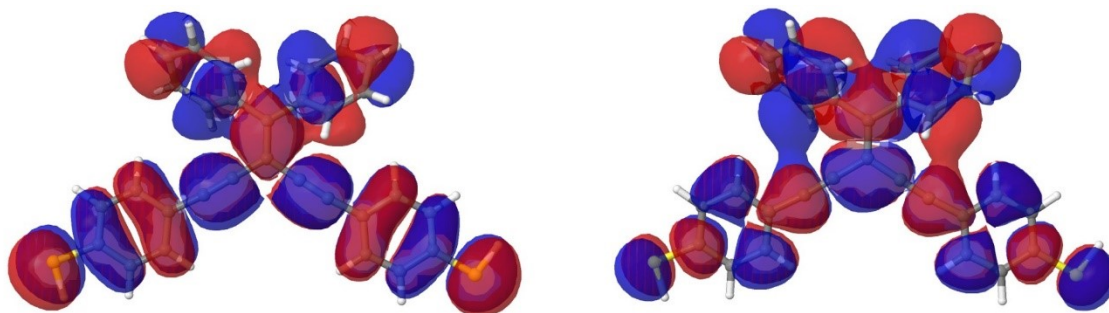


Fig. S31 HOMO (left) and LUMO (right) orbitals of molecule **1b** [as the thiol (SH) derivative].

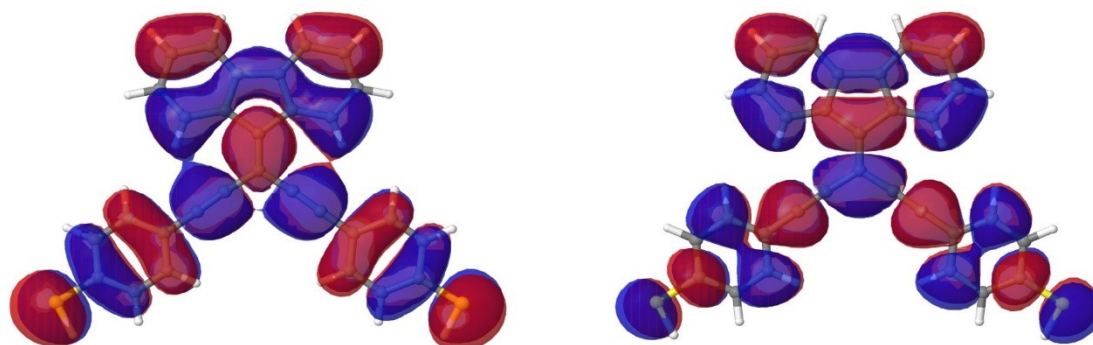


Fig. S32 HOMO (left) and LUMO (right) orbitals of molecule **2b** [as the thiol (SH) derivative].

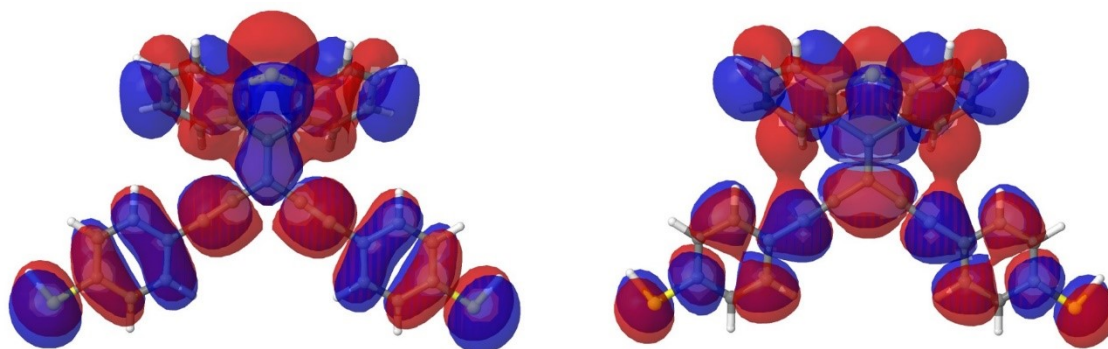


Fig. S33 HOMO (left) and LUMO (right) orbitals of molecule **3b** [as the thiol (SH) derivative].

S9. Energy levels, ionization potential and electron affinity

The ionization potential (IP) is calculated using the formula $IP=E(N-1)-E(N)$ and the electron affinity using the formula $EA=E(N)-E(N+1)$. Where, E is the ground state energy of the molecule and N is the number of electrons.

Table S5 HOMO and LUMO energy levels, IP and EA for molecules **1-4a** and **1-3b**.

	HOMO (eV)	LUMO (eV)	IP (eV)	EA (eV)
1a	-4.4	-2.6	5.9	1.0
2a	-4.6	-3.0	6.0	1.4
3a	-4.4	-2.6	5.8	1.1
4	-4.4	-2.1	6.0	0.4
1b	-4.6	-2.7	6.1	1.1
2b	-4.7	-3.1	6.2	1.5
3b	-4.5	-2.7	6.0	1.2

S10. Binding Energy

To model the expected behaviour in a molecular junction, the binding energy between the molecules **1-3a**, **4** and **1-3b** and a (111) gold surface was calculated. In the case of geometry 1 the molecules bind through the terminal anchor which are either SMe groups or S (derived from SAc).

Table S6. Theoretical electrode separation for the optimum geometries of molecules **1-3A** and **1-3B** for the two configurations shown in Fig. 4.

	1A	2A	3A	1B	2B	3B
Configuration 1 (nm)	1.66	1.70	1.62	1.45	1.55	1.42
Configuration 2 (nm)	1.34	1.53	1.43	1.33	1.48	1.37

Typically SMe groups bind stronger to a surface adatom than to a flat surface¹², therefore we calculated the binding between the molecule and an adatom on a surface and the terminal sulfur atom as shown in Figure 4a. Here the single gold electrode consists of three layers of (111) gold. The system was treated as a two-component object, where the gold electrode is A and the molecule is B. Due to basis set superposition errors (BSSE), when using a localized basis set we used a counterpoise method to evaluate the binding energy E_{Bind} . This is given by the following equation:

$$E_{\text{Bind}} = E_{AB}^{AB} - (E_A^{AB} + E_B^{AB})$$

where E_{AB}^{AB} is the ground state energy of the gold electrode (A) and molecule (B), E_A^{AB} is the energy of the gold (A) in the basis of the dimer AB and E_B^{AB} is the energy of the molecule in

the basis of the dimer AB. The parameters d (Au-S distance), θ (tilt angle) and Φ (rotation angle) were changed to find the optimum binding geometry. Fig. S34 shows a comparison in the binding energy for two different orientations of the SMe anchor groups of **1a**. The optimum geometry has the methyl groups aligned with the plane of the molecule as seen in Fig. S27, however the binding energy is greater when the methyl groups are rotated out of the plane by 90° . This is also the case for **2a**, **3a** and **4**. For molecules **1b**, **2b** and **3b** the C(O)Me protecting group was removed from the terminal sulfurs.

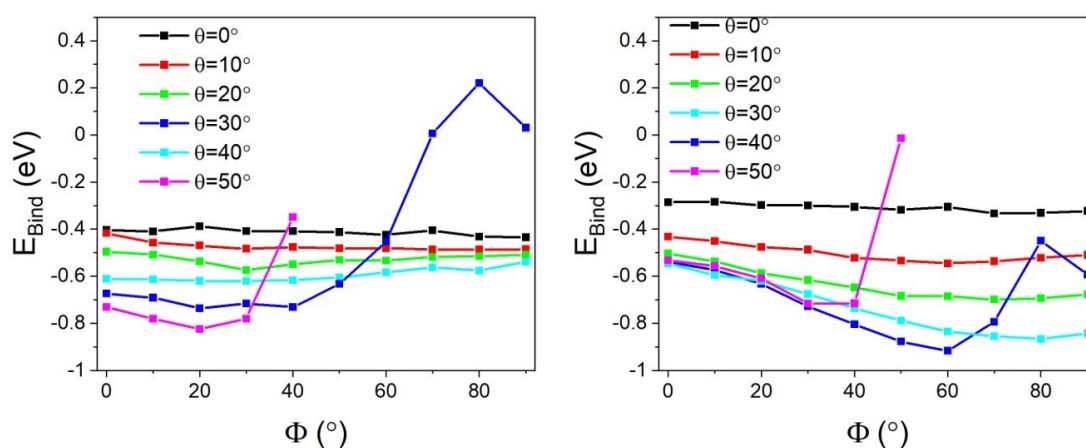


Fig. S34 (Left) Binding energy E_{Bind} of molecule **1a** SMe groups aligned with plane of molecule against rotation angle Φ for tilt angle θ between 0 and 50° contacted to an adatom on a gold (111) surface. (Right) **1a** with SMe groups rotated 90° out of the plane of the molecule.

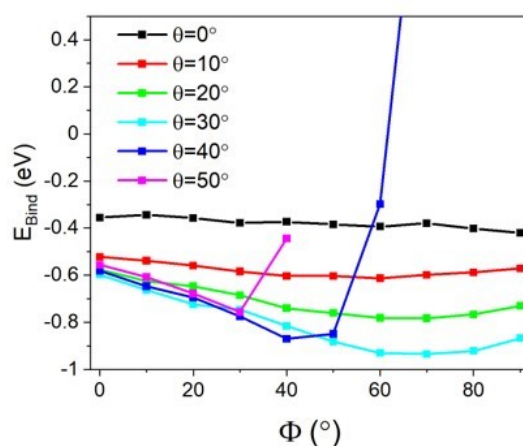


Fig. S35 Binding energy E_{Bind} of molecule **2a** with SMe groups rotated 90° out of the plane of the molecule against rotation angle Φ for tilt angle θ between 0 and 50° contacted to an adatom on a gold (111) surface.

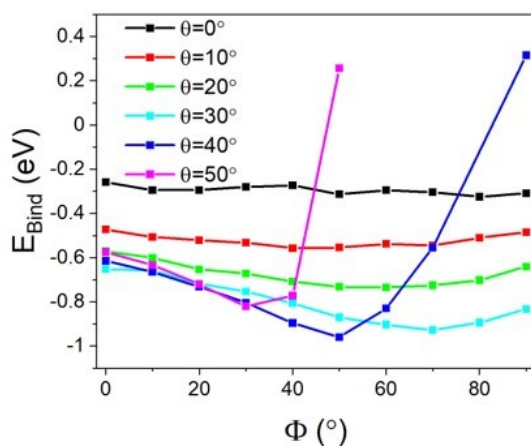


Fig. S36 Binding energy E_{Bind} of molecule **3a** with SMe groups rotated 90° out of the plane of the molecule against rotation angle Φ for tilt angle θ between 0 and 50° contacted to an adatom on a gold (111) surface.

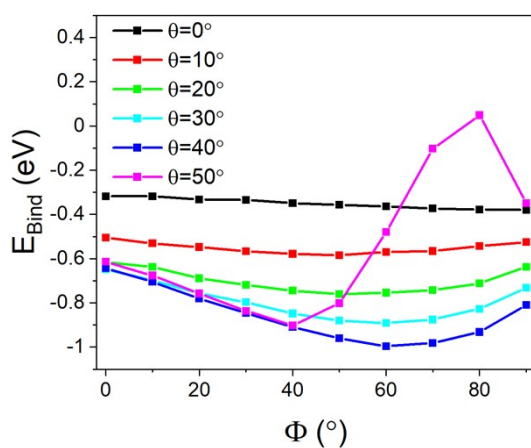


Fig. S37 Binding energy E_{Bind} of molecule **4** with SMe groups rotated 90° out of the plane of the molecule against rotation angle Φ for tilt angle θ between 0 and 50° contacted to an adatom on a gold (111) surface.

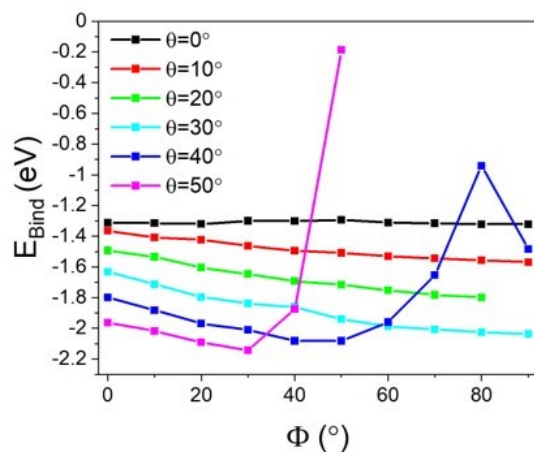


Fig. S38 Binding energy E_{Bind} of molecule **1b** against rotation angle Φ for tilt angle θ between 0 and 50° contacted to an adatom on a gold (111) surface.

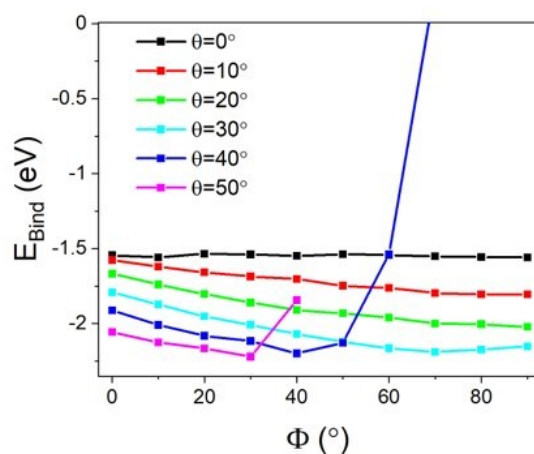


Fig. S39 Binding energy E_{Bind} of molecule **2b** against rotation angle Φ for tilt angle θ between 0 and 50° contacted to an adatom on a gold (111) surface.

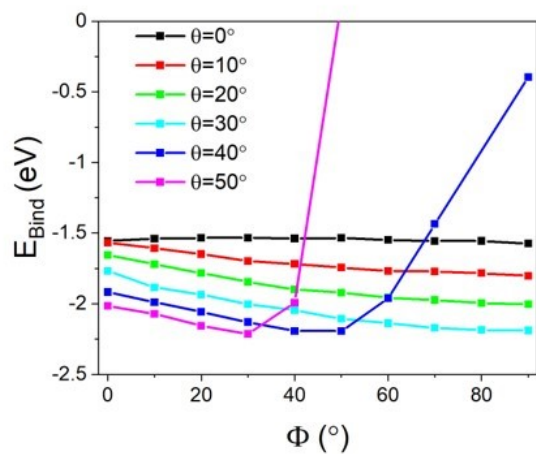


Fig. S40 Binding energy E_{Bind} of molecule **3b** against rotation angle Φ for tilt angle θ between 0 and 50° contacted to an adatom on a gold (111) surface.

S11. Transmission Coefficients

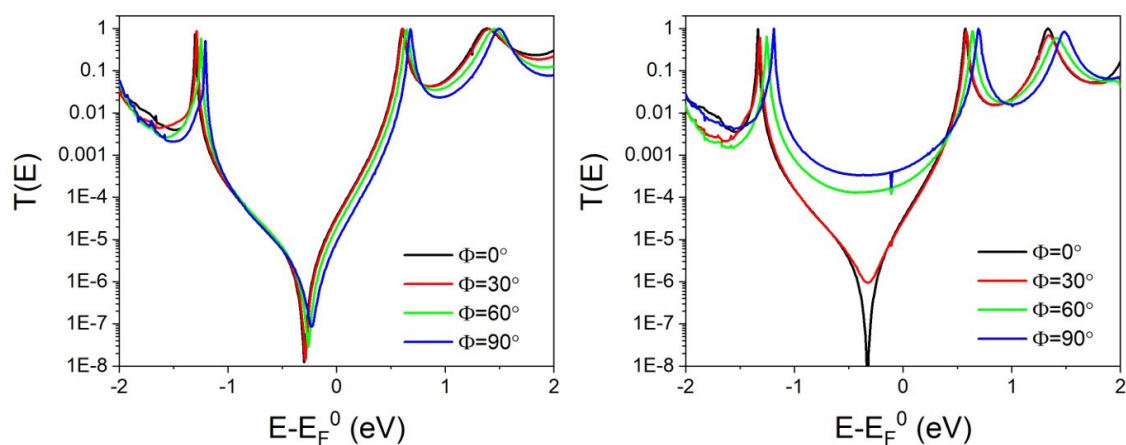


Fig. S41 Zero bias transmission coefficient $T(E)$ versus electron energy of molecule **1a** in configuration 1 for varying rotation angles Φ at tilt angles of $\theta=20^\circ$ (left) and $\theta=40^\circ$ (right).

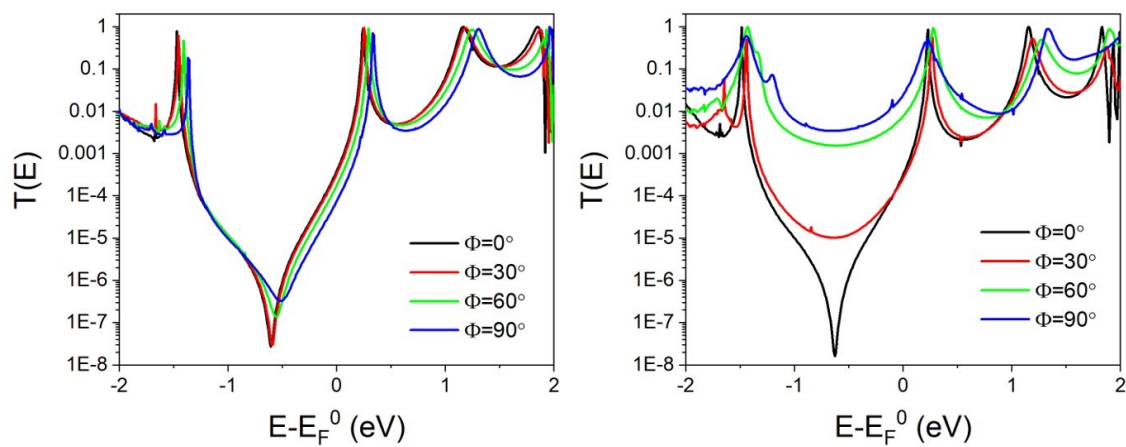


Fig. S42 Zero bias transmission coefficient $T(E)$ versus electron energy of molecule **2a** in configuration 1 for varying rotation angles Φ at tilt angles of $\theta=20^\circ$ (left) and $\theta=40^\circ$ (right).

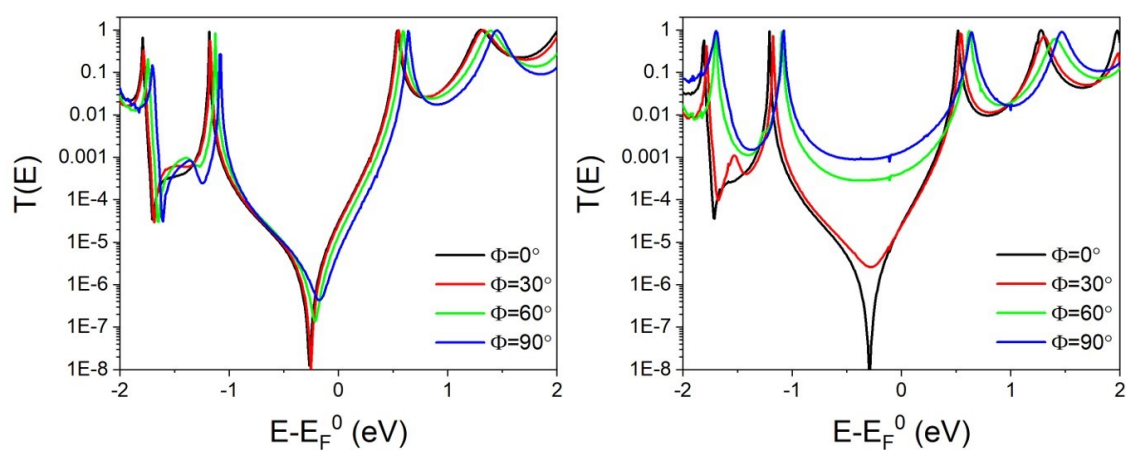


Fig. S43 Zero bias transmission coefficient $T(E)$ versus electron energy of molecule **3a** in configuration 1 for varying rotation angles Φ at tilt angles of $\theta=20^\circ$ (left) and $\theta=40^\circ$ (right).

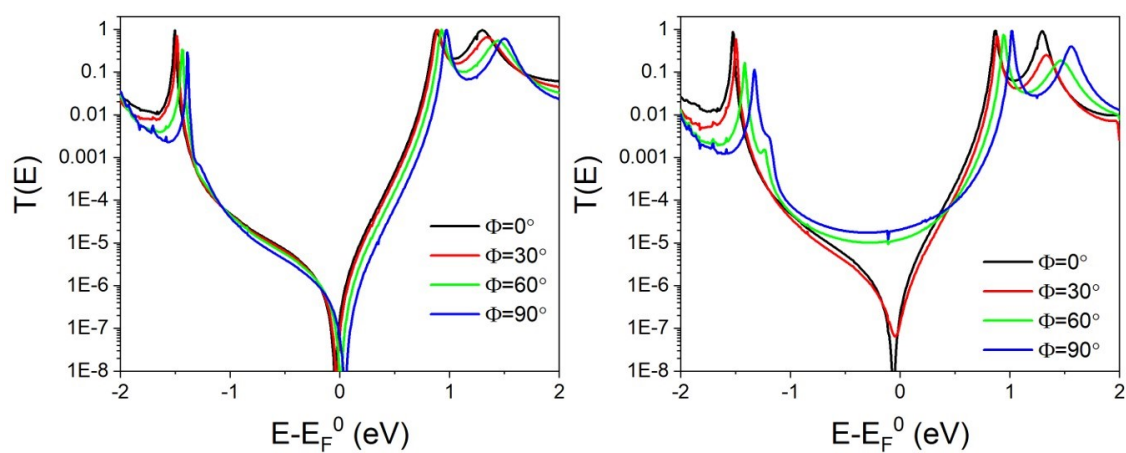


Fig. S44 Zero bias transmission coefficient $T(E)$ versus electron energy of molecule **4a** in configuration 1 for varying rotation angles Φ at tilt angles of $\theta=20^\circ$ (left) and $\theta=40^\circ$ (right).

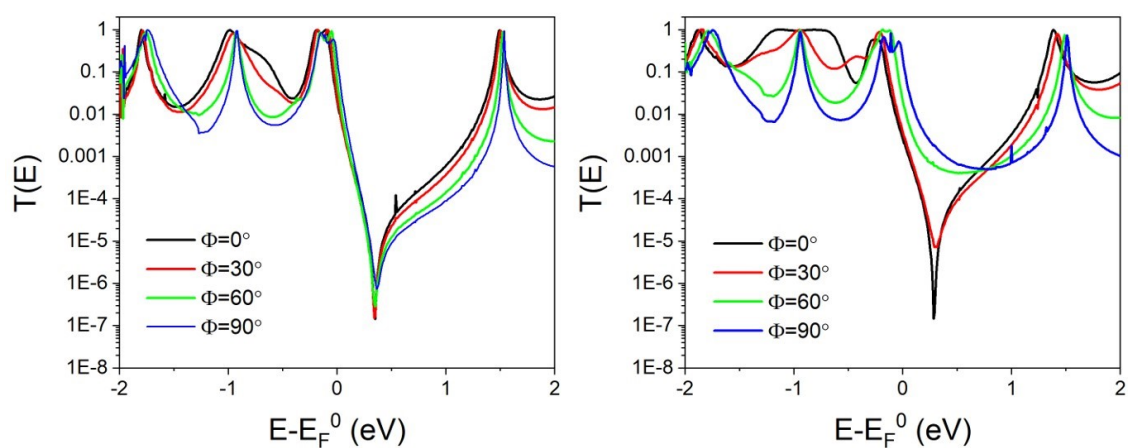


Fig. S45 Zero bias transmission coefficient $T(E)$ versus electron energy of molecule **1b** in configuration 1 for varying rotation angles Φ at tilt angles of $\theta=20^\circ$ (left) and $\theta=40^\circ$ (right).

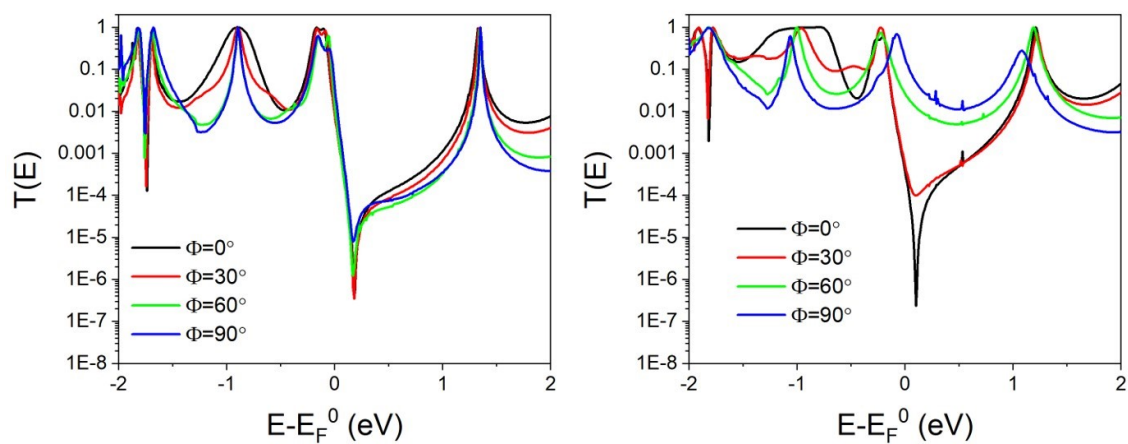


Fig. S46 Zero bias transmission coefficient $T(E)$ versus electron energy of molecule **2b** in configuration 1 for varying rotation angles Φ at tilt angles of $\theta=20^\circ$ (left) and $\theta=40^\circ$ (right).

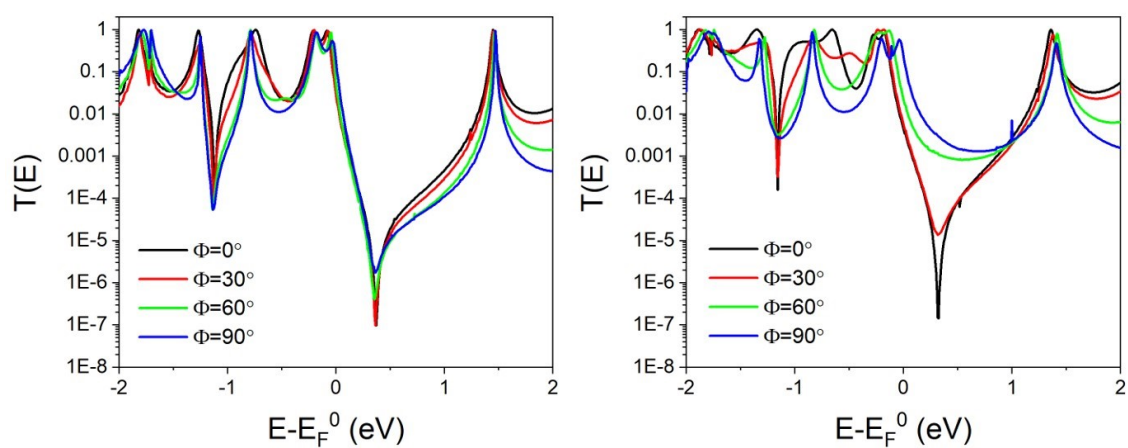


Fig. S47 Zero bias transmission coefficient $T(E)$ versus electron energy of molecule **3b** in configuration 1 for varying rotation angles Φ at tilt angles of $\theta=20^\circ$ (left) and $\theta=40^\circ$ (right).

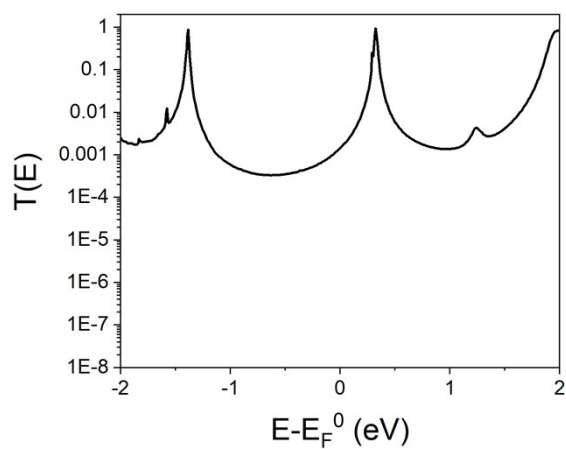


Fig. S48 Zero bias transmission coefficient $T(E)$ versus electron energy of molecule **2a** in configuration 2.

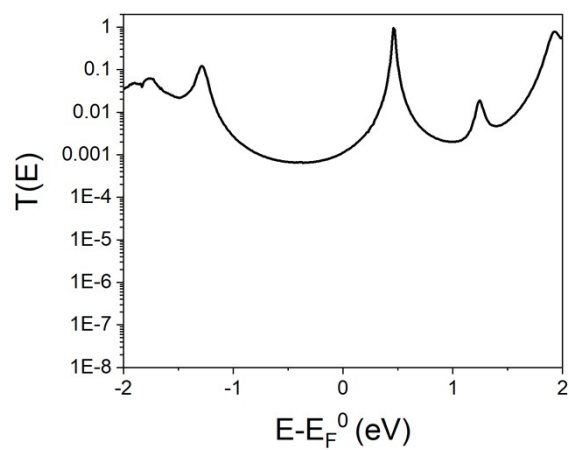


Fig. S49 Zero bias transmission coefficient $T(E)$ versus electron energy of molecule **3a** in configuration 2.

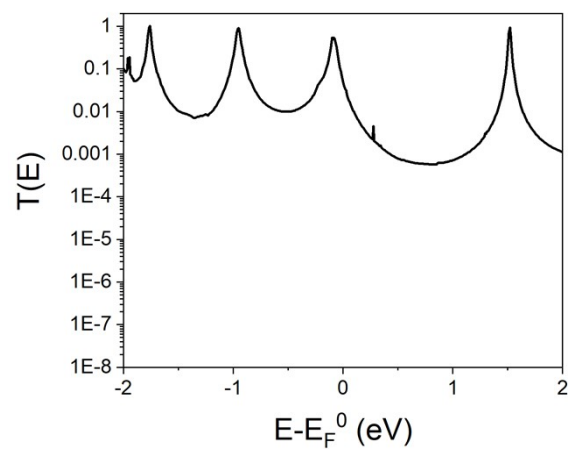


Fig. S50 Zero bias transmission coefficient $T(E)$ versus electron energy of molecule **1b** in configuration 2.

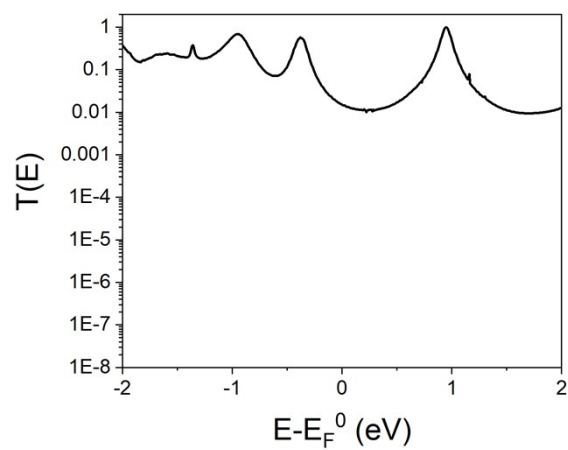


Fig. S51 Zero bias transmission coefficient $T(E)$ versus electron energy of molecule **2b** in configuration 2.

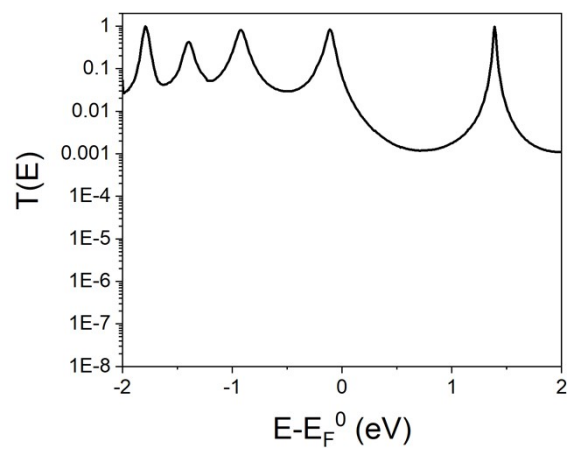


Fig. S52 Zero bias transmission coefficient $T(E)$ versus electron energy of molecule **3b** in configuration 2.

S12. Conductance and Seebeck Coefficient calculations for configuration 1

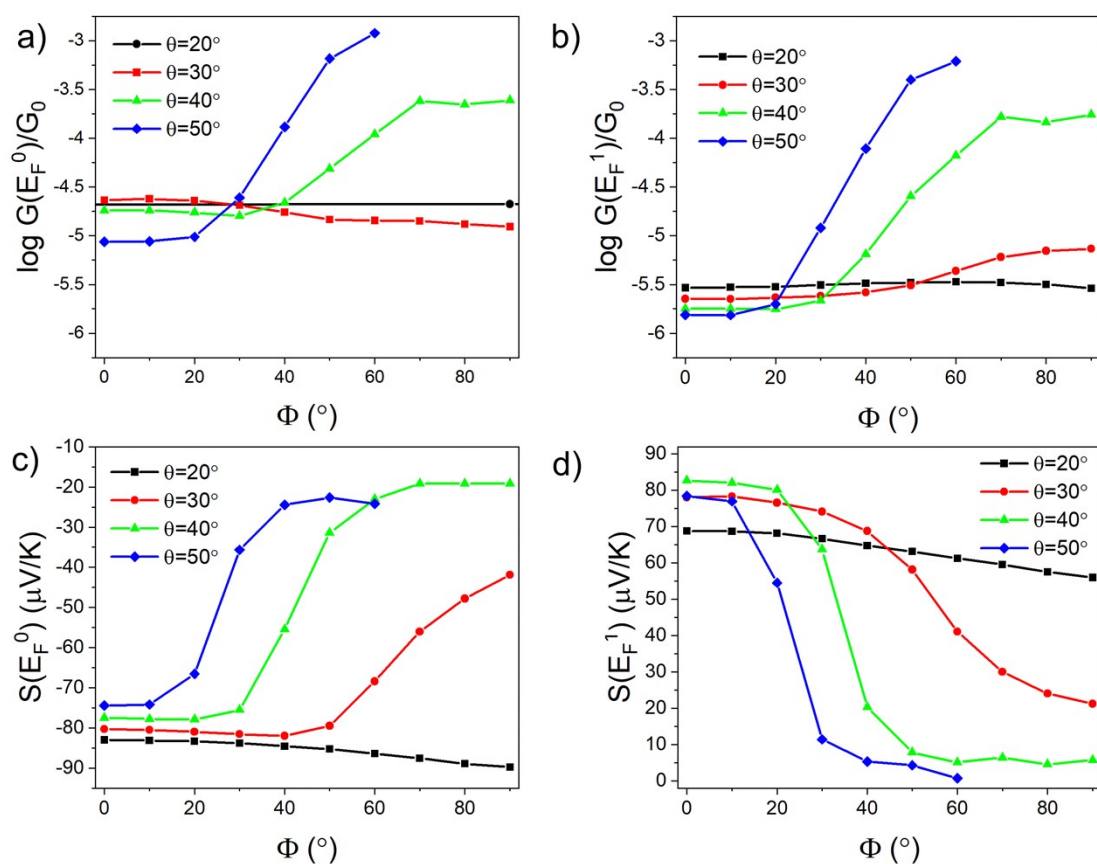


Fig. S53 (a) Conductance of molecule **1a** as a function of the rotation angle Φ , for tilt angles θ between 20 and 50° evaluated at E_F^0 and (b) $E_F^1 = E_F^0 - 0.5$ eV. (c) Seebeck coefficient of molecule **1a** as a function of the rotation angle Φ , for tilt angles θ between 20 and 50° evaluated at E_F^0 and (d) $E_F^1 = E_F^0 - 0.5$ eV.

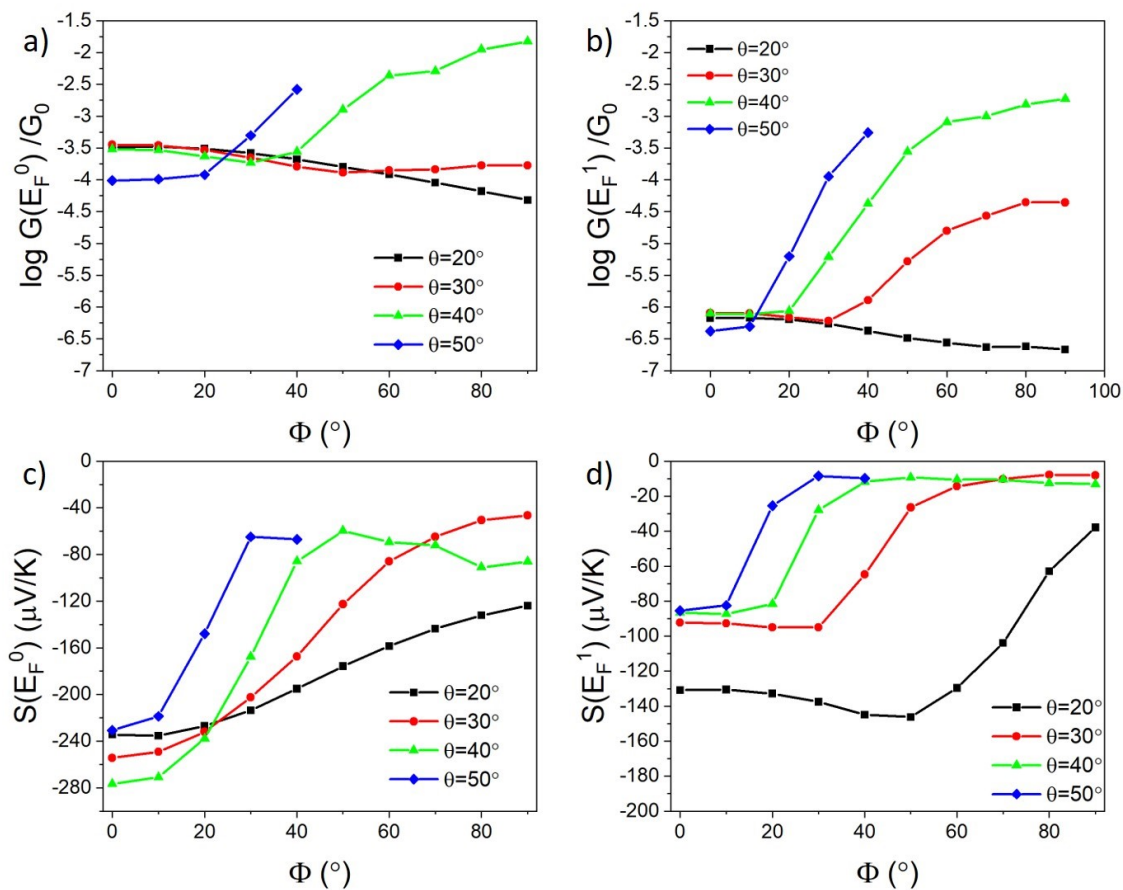


Fig. S54 (a) Conductance of molecule **2a** as a function of the rotation angle Φ , for tilt angles θ between 20 and 50° evaluated at E_F^0 and (b) $E_F^1 = E_F^0 - 0.5$ eV. (c) Seebeck coefficient of molecule **2a** as a function of the rotation angle Φ , for tilt angles θ between 20 and 50° evaluated at E_F^0 and (d) $E_F^1 = E_F^0 - 0.5$ eV.

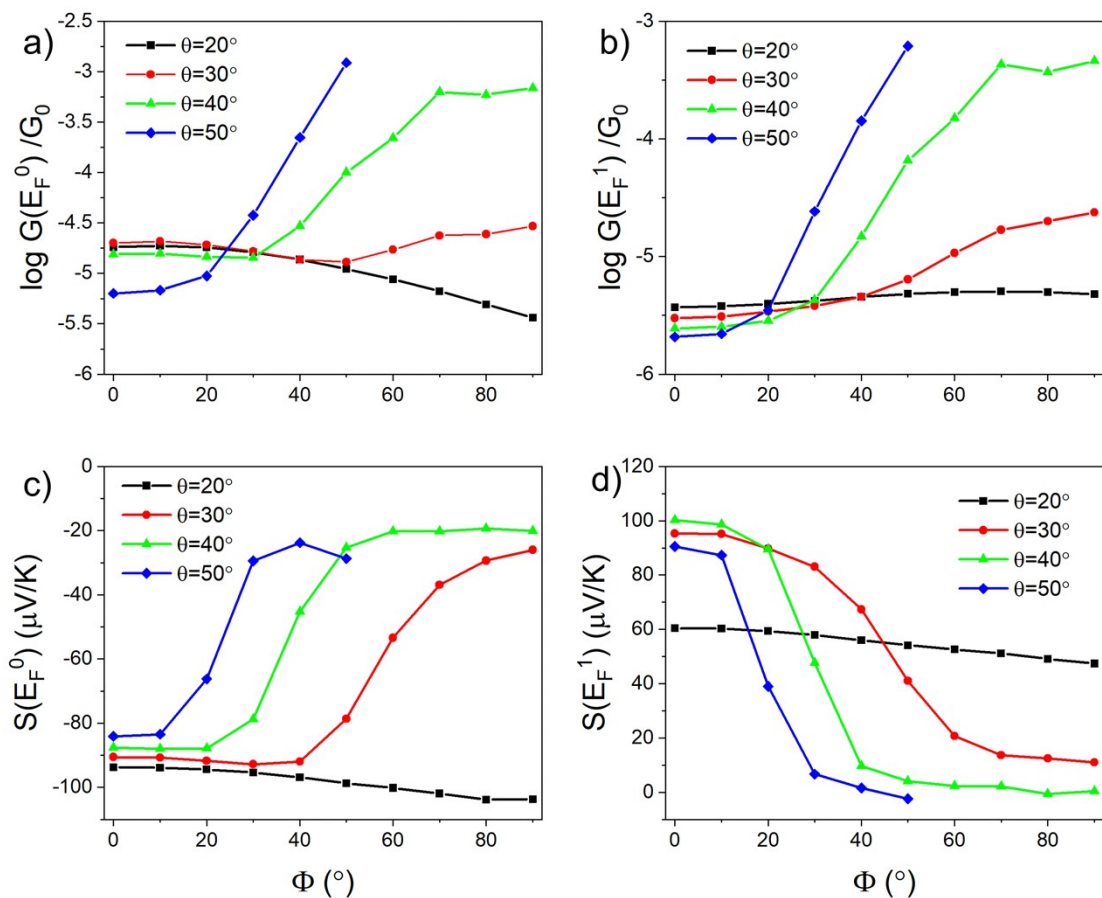


Fig. S55 (a) Conductance of molecule **3a** as a function of the rotation angle Φ , for tilt angles θ between 20 and 50° evaluated at E_F^0 and (b) $E_F^1 = E_F^0 - 0.5$ eV. (c) Seebeck coefficient of molecule **3a** as a function of the rotation angle Φ , for tilt angles θ between 20 and 50° evaluated at E_F^0 and (d) $E_F^1 = E_F^0 - 0.5$ eV.

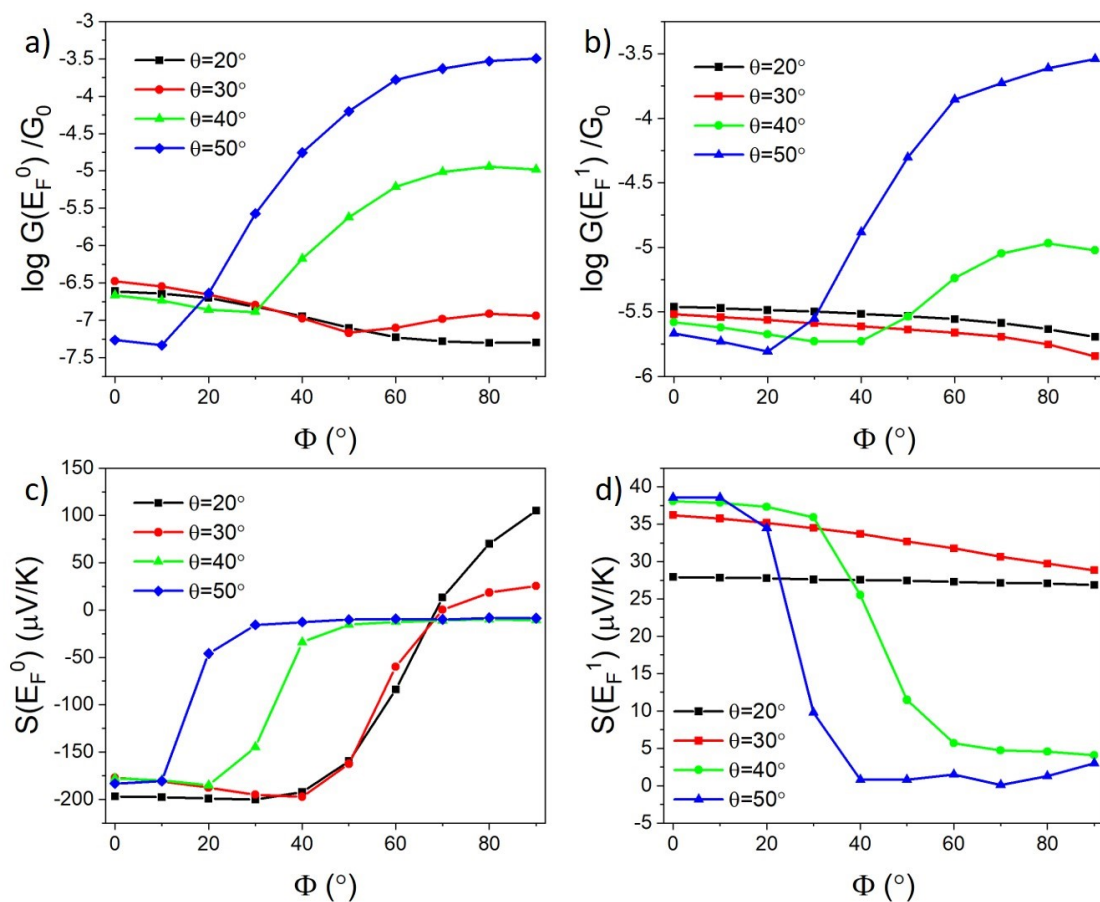


Fig. S56 (a) Conductance of molecule **4** as a function of the rotation angle Φ , for tilt angles θ between 20 and 50° evaluated at E_F^0 and (b) $E_F^1=E_F^0-0.5$ eV. (c) Seebeck coefficient of molecule **4** as a function of the rotation angle Φ , for tilt angles θ between 20 and 50° evaluated at E_F^0 and (d) $E_F^1=E_F^0-0.5$ eV.

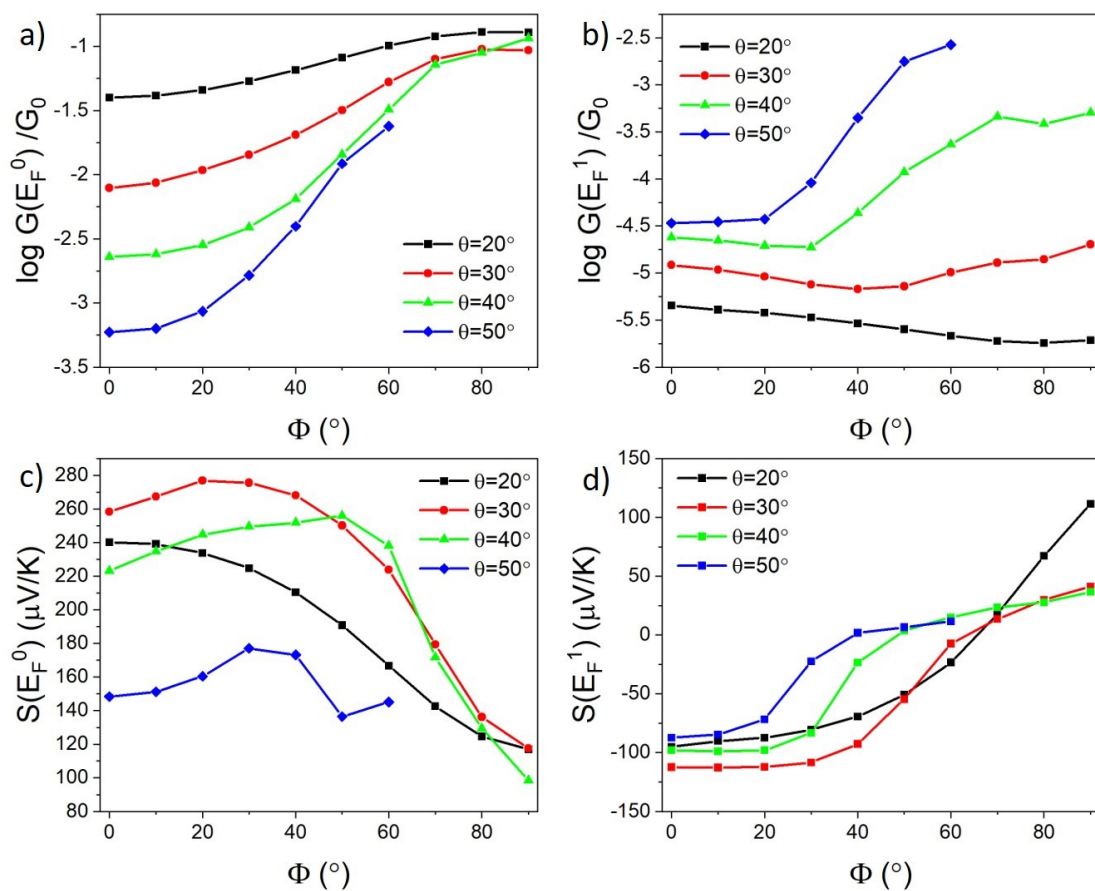


Fig. S57 (a) Conductance of molecule **1b** as a function of the rotation angle Φ , for tilt angles θ between 20 and 50° evaluated at E_F^0 and (b) $E_F^1 = E_F^0 - 0.5$ eV. (c) Seebeck coefficient of molecule **1b** as a function of the rotation angle Φ , for tilt angles θ between 20 and 50° evaluated at E_F^0 and (d) $E_F^1 = E_F^0 + 0.4$ eV.

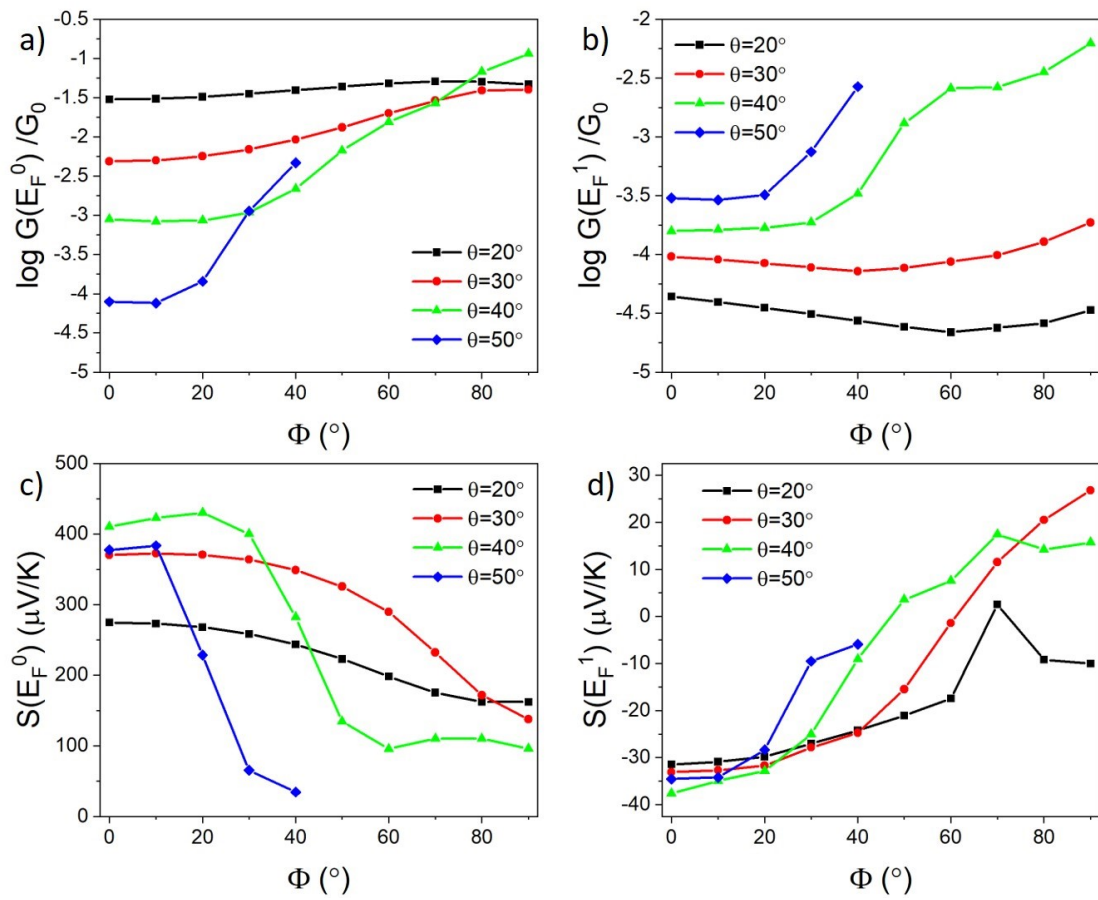


Fig. S58 (a) Conductance of molecule **2b** as a function of the rotation angle Φ , for tilt angles θ between 20 and 50° evaluated at E_F^0 and (b) $E_F^1 = E_F^0 - 0.5$ eV. (c) Seebeck coefficient of molecule **2b** as a function of the rotation angle Φ , for tilt angles θ between 20 and 50° evaluated at E_F^0 and (d) $E_F^1 = E_F^0 + 0.4$ eV.

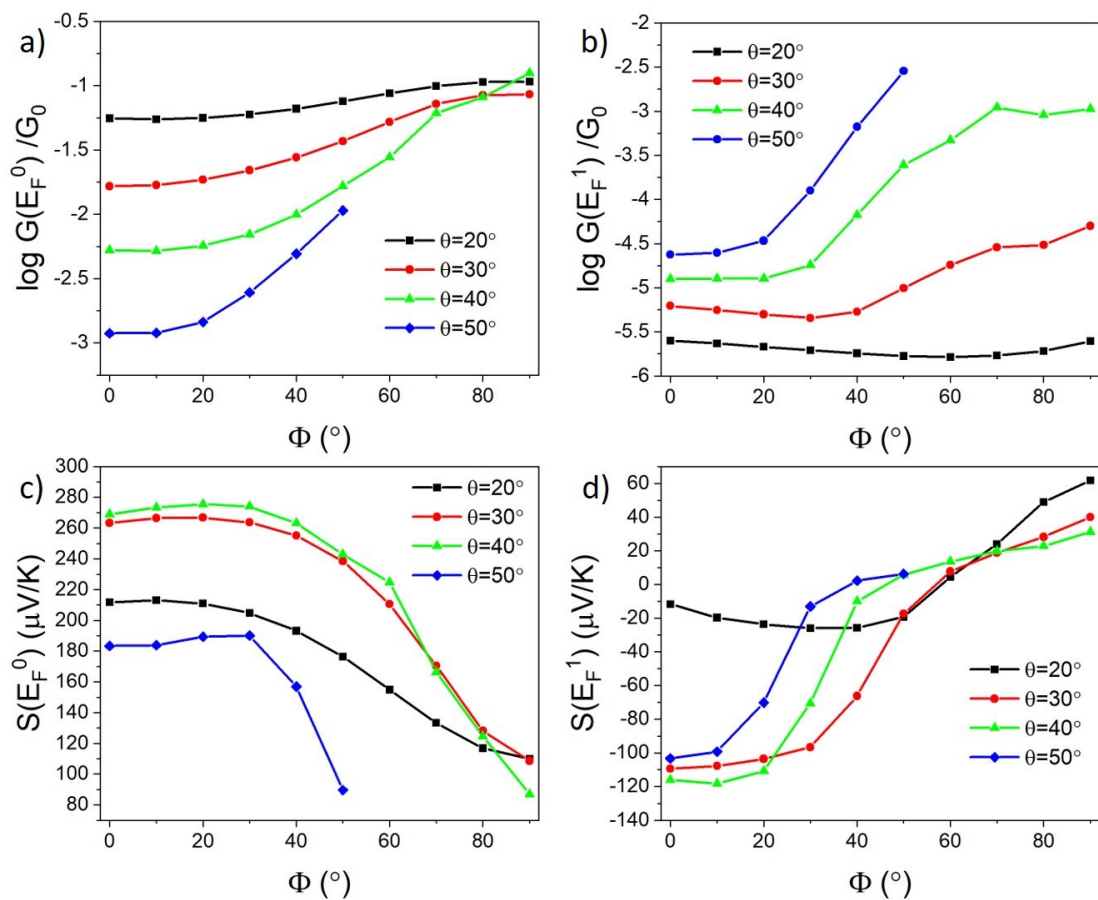


Fig. S59 (a) Conductance of molecule **3b** as a function of the rotation angle Φ , for tilt angles θ between 20 and 50° evaluated at E_F^0 and (b) $E_F^1 = E_F^0 - 0.5$ eV. (c) Seebeck coefficient of molecule **3b** as a function of the rotation angle Φ , for tilt angles θ between 20 and 50° evaluated at E_F^0 and (d) $E_F^1 = E_F^0 + 0.4$ eV.

S13. Conductance Calculations for configuration 2

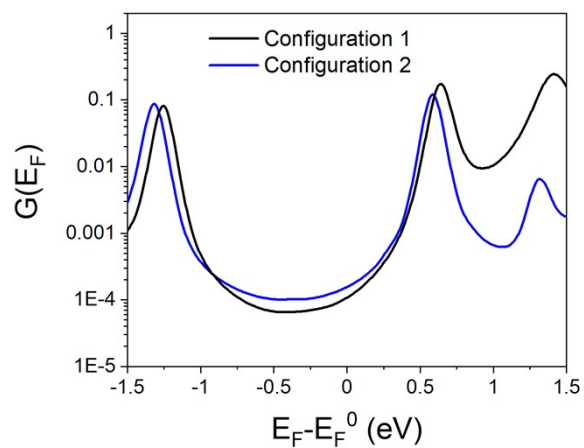


Fig. S60 Conductance as a function of E_F for molecule **1a** in configurations 1 and 2.

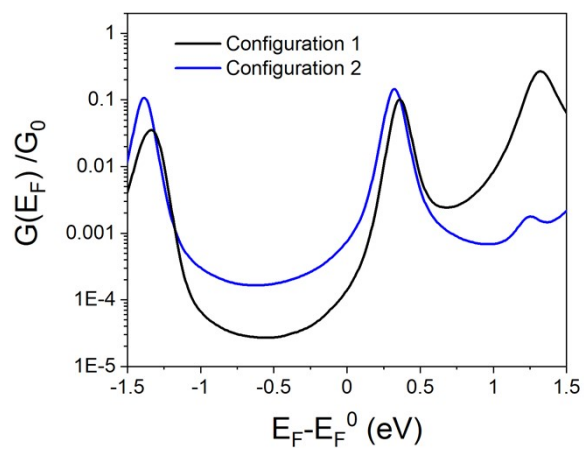


Fig. S61 Conductance as a function of E_F for molecule **2a** in configurations 1 and 2.

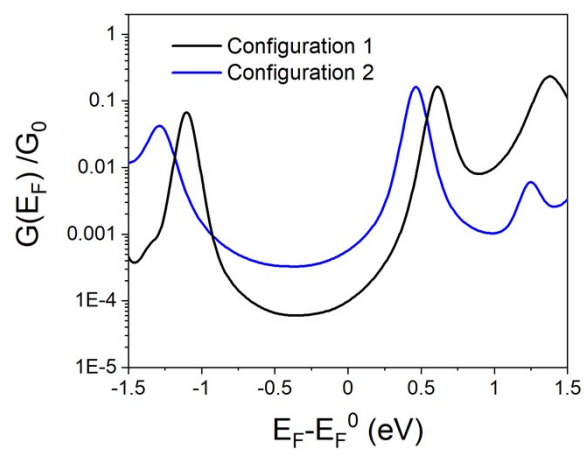


Fig. S62 Conductance as a function of E_F for molecule **3a** in configurations 1 and 2.

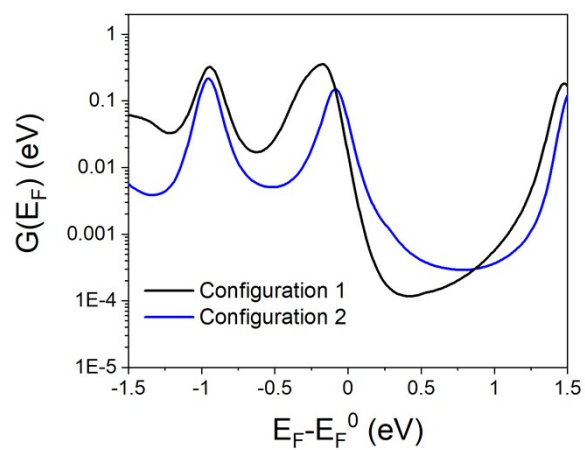


Fig. S63 Conductance as a function of E_F for molecule **1b** in configurations 1 and 2.

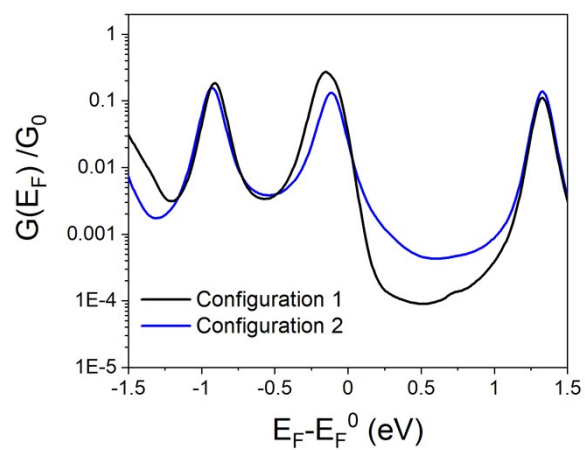


Fig. S64 Conductance as a function of E_F for molecule **2b** in configurations 1 and 2.

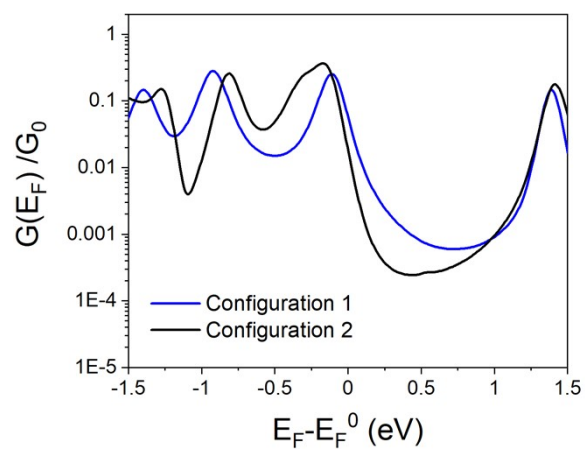


Fig. S65 Conductance as a function of E_F for molecule **3b** in configurations 1 and 2.

c) References for SI

- 1 G. F. Zhang, Z. Q. Chen, M. P. Aldred, Z. Hu, T. Chen, Z. Huang, X. Meng and M. Q. Zhu, *Chemical Communications*, 2014, **50**, 12058–12060.
- 2 G. F. Zhang, M. P. Aldred, Z. Q. Chen, T. Chen, X. Meng and M. Q. Zhu, *RSC Advances*, 2015, **5**, 1079–1082.
- 3 P. M. Donovan and L. T. Scott, *Journal of the American Chemical Society*, 2004, **126**, 3108–3112.
- 4 M. S. Inkpen, A. J. P. White, T. Albrecht and N. J. Long, *Dalton Transactions*, 2014, **43**, 15287–15290.
- 5 Y. Q. Sun, J. He, Z. Xu, G. Huang, X. P. Zhou, M. Zeller and A. D. Hunter, *Chemical Communications*, 2007, **45**, 4779–4781.
- 6 L. Krause, R. Herbst-Irmer, G. M. Sheldrick and D. Stalke, *Journal of Applied Crystallography*, 2015, **48**, 3–10.
- 7 G. M. Sheldrick, *Acta Crystallographica Section C: Structural Chemistry*, 2015, **71**, 3–8.
- 8 O. V. Dolomanov, L. J. Bourhis, R. J. Gildea, J. A. K. Howard and H. Puschmann, *Journal of Applied Crystallography*, 2009, **42**, 339–341.
- 9 S. Toyota, *Chemical Reviews*, 2010, **110**, 5398–5424.
- 10 N. Treitel, L. Eshdat, T. Sheradsky, P. M. Donovan, R. R. Tykwinski, L. T. Scott, H. Hopf and M. Rabinovitz, *Journal of the American Chemical Society*, 2006, **128**, 4703–4709.
- 11 C. R. Arroyo, E. Leary, A. Castellanos-Gómez, G. Rubio-Bollinger, M. T. González and N. Agraït, *Journal of the American Chemical Society*, 2011, **133**, 14313–14319.
- 12 M. S. Inkpen, Z. -F Liu, H. Li, L. M. Campos, J. B. Neaton and L. Venkataraman, *Nature Chemistry*, 2019, **11**, 351–358.